Chapter 10

Fiber-laser-generated Noise-like Pulses and Their Applications

Ci-Ling Pan, Alexey Zaytsev, Yi-Jing You and Chih-Hsuan Lin

Additional information is available at the end of the chapter

http://dx.doi.org/10.5772/61856

Abstract

We describe generation and amplification of medium- and high-energy noise-like pulses (NLPs) using Yb-doped optical fibers. We also demonstrate supercontinuum (SC) generation techniques in which NLPs serve as the pump. SC pumped by NLPs has been employed successfully in optical coherence tomography systems.

Keywords: Yb-doped fiber laser, laser amplifier, ultrafast laser, noise-like pulse, supercontinuum generation, nonlinear optics, optical coherence, tomography

1. Introduction

In the past two decades, ultrafast fiber laser has been a field that witnessed rapid development of the technology and emergent applications. Ultrafast pulses at high average power are useful in numerous application areas including micromachining and material processing, nonlinear frequency conversion, biomedical application, and fundamental science. It is generally recognized that fiber laser is an attractive technology for compact, robust, low cost, and reliable ultrafast pulse sources. Compared with conventional bulk solid-state lasers, main advantages of fiber-based laser systems include good beam quality, ease of delivery, and excellent heat-dissipation properties. The last feature is due to the large surface area-active volume ratio of optical fibers.

Rare-earth-doped fiber lasers also exhibit much higher efficiency than crystalline solid-state lasers. Since the first rare-earth-doped fiber laser was invented over 50 years ago [1], many experimental and theoretical results on silica- and fluoride-doped fiber amplifiers and lasers with various rare-earth dopants have been reported [2–4]. The commercially available erbium-doped amplifiers have already established their key role for optical communication networks

at 1.55-μm. On the other hand, high average power ultrafast laser sources emitting in the 1-μm wavelength range, i.e., ytterbium-doped fiber laser, have also attracted much attention.

Ultrafast pulsed fiber lasers have been observed to operate in different mode-locking regimes, such as soliton, similariton, and dissipative soliton. A special regime of repetitively pulsed fiber laser, i.e., lasers generating the so-called noise-like pulses or NLPs [4–8], was also reported. NLPs are relatively long (sub-ns) wave packets, which exhibit a fine inner structure of sub-ps pulses with randomly varying amplitude and duration. Depending on settings of polarizing components such as the wave plates, fiber lasers can generate both regular mode-locked pulses (MLPs) and NLPs. The first demonstration of fiber lasers generating NLPs was that of a ring-cavity Er: doped fiber oscillator [9]. Later on, different cavity configurations and active media were employed to achieve NLPs with controllable characteristics.

In this chapter, we describe our recent work on generation and amplification of medium- and high-energy NLPs with Yb-doped fibers. We also demonstrate supercontinuum (SC) generation techniques where NLPs serve as the pump. Theoretical aspects as well as discussions about physical mechanisms, which make NLPs distinguishable from regular MLPs, are also included. SC pumped by NLPs has been employed successfully in optical coherence tomography (OCT) systems. The advantages of the present approach using NLPs will be discussed herein.

We first describe, analyze, and compare two popular cavity configurations for generating NLPs: a dispersion-mapped cavity and an all-normal dispersion (ANDi). Simulation results based on coupled nonlinear Schrödinger equations are supported by experiments. Nonlinear polarization evolution (NPE) is the main mechanism for pulsed operation in these lasers. We show that both regular Gaussian pulses and NLPs can be achieved in the same cavity by choosing proper cavity components and adjustment.

The second part of the chapter is about SC generation. Here, we analyze the possibilities of efficient SC generation using NLPs propagating in standard silica fibers. It is shown that unique features of NLPs make them very useful for such a purpose. That is, the central wavelength of the pump and zero-dispersion wavelength (ZDW) of SC generation media are not critical. We show that, even if the pump wavelength is deep in the normal dispersion regime (for example, ~1 μm where ZDW = 1.33 μm), SC can be efficiently generated. Simulations and experimental results of SC generation by NLPs using different single-mode fibers (SMFs) are presented. We discuss the optimal selection of fiber types and other characteristics to generate flat SC in spectral region above 1 μm. The pros and cons of using specialty fibers such as photonic crystal fibers (PCFs) pumped by NLPs will also be elaborated.

In the third part of the chapter, we consider the application of SC generated by NLPs for selected applications, i.e., OCT. The SC spectrum is flat with a bandwidth of 365 nm centered at 1320 nm. The light source is successfully employed in a time-domain OCT (TD-OCT) scheme, achieving an axial resolution of 2.3 μm. High-resolution fiber-based spectral-domain OCT (SD-OCT) imaging of bio-tissue (onion skin), comparable to that obtained using a commercial swept source, is also demonstrated.

http://dx.doi.org/10.5772/61856

2. NLP generation with fiber lasers

NLPs were first demonstrated by Horowitz *et al.* from an Er-doped mode-locked fiber laser in 1997 [9]. A NLP is defined as some kind of complicated waveform of relatively long (sub-nanosecond) duration. It also exhibits a fine inner structure of much narrow sub-pulses (a few hundred femtoseconds in width) with randomly varying intensity and duration. The inner structure varies from one waveform to another in the pulse train. On the other hand, the repetition rate and average duration of the aforementioned waveforms forming a train of pulses are relatively stable. It was found and demonstrated that such kinds of pulses have some interesting common features: (1) a very large optical bandwidth (usually of several tens of nanometers); (2) specific waveforms that exhibit a double-scaled average autocorrelation trace with a narrow peak riding on a wide pedestal; and (3) low temporal coherence. Moreover, it was found that NLPs are essentially undistorted even after the pulses have propagated through a lengthy dispersive medium, e.g., an optical fiber over a long distance.

Thus far, characteristics of fiber-based NLPs have been predominantly assessed only indirectly by means of numerical simulation or average measurements. There have been many works published on NLPs generated by fiber laser, but still there is a lack of simple qualitative explanation of physical mechanisms involved in the formation of NLPs till now. In a paper by Horowitz *et al.*, it was supposed that NLPs are caused by a polarization-dependent delay effect due to the birefringence in the laser cavity [9]. Smirnov *et al.* [10], however, demonstrated that NLP still can occur in weakly birefringent fiber laser systems. In this paper [10], the authors introduced three regimes of single pulse generation in an ANDi fiber laser. The same regimes can also be observed in our dispersion-mapped fiber laser. On the other hand, Tang *et al.* concluded that the key physical mechanism of noise-like generation is caused by the combined effect of the soliton collapse and cavity positive feedback for dispersion managed fiber lasers [11]. This contradicted with the report that NLPs are generated in an ANDi fiber laser [12]. Aguergaray *et al.*, meanwhile, proposed that NLPs are caused by the Raman-driven destabilization of mode-locked long-cavity fiber lasers. The destabilization is accompanied by the emergence of a strong frequency-downshifted stokes signal [13]. Therefore, there are several mechanisms that can lead to the generation of NLPs. In our dispersion-mapped and ANDi Yb-doped fiber lasers, we did observe Raman peaks in the output spectra [14]. Hence, Aguergaray's model is probably more suitable for our laser systems.

2.1. NLPs generated by a dispersion-mapped fiber laser

The configuration of this laser is shown in Figure 1. It is similar to the design of stretched pulse mode-locked lasers [15]. The laser cavity comprises a segment of single-mode silica fiber followed by a length of Yb-doped fiber (Yb1200-10/125DC, Liekki). A set of 915 nm laser diodes with total power up to 24 W and a power combiner are used for pumping. Nonlinear polarization rotation (NPE) is implemented by a polarization beam splitter (PBS) and wave plates. A grating pair in the near-Littrow configuration is placed after the PBS to provide negative dispersion in the cavity. The grating arrangement functions as a dispersive delay line (DDL). The net group velocity dispersion (GVD) of the cavity is kept slightly positive. An optical

isolator is placed in the air space to ensure unidirectional operation of the laser so that the mode-locking process is self-starting. By adjusting the wave plates, stable mode-locked or NLPs are readily observed. The output can be taken directly from the NPE ejection port. Additional information about the laser can be found in Ref. [14].

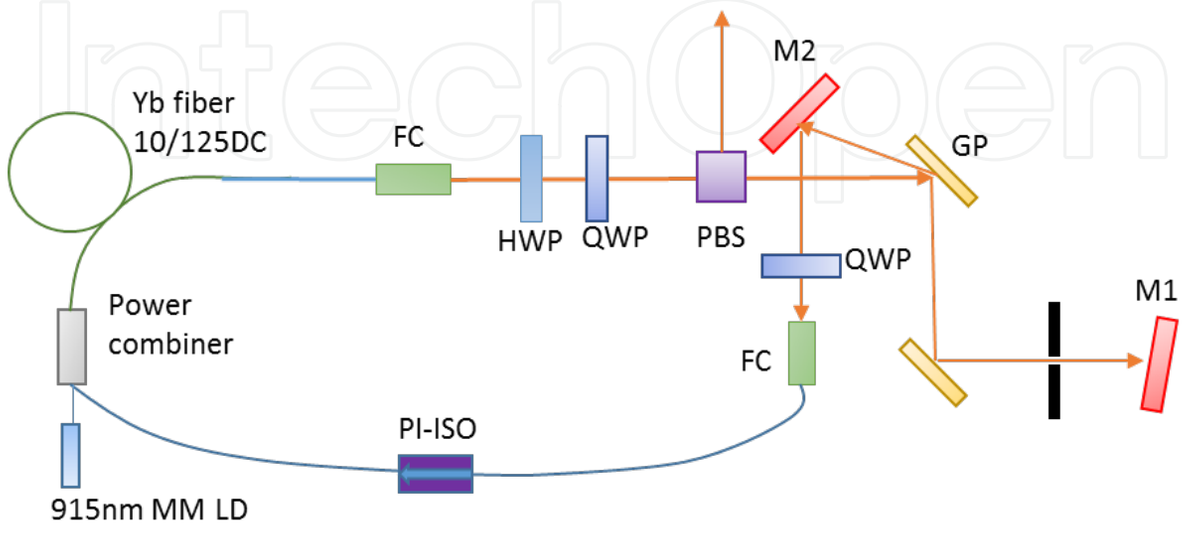

Figure 1. Schematic of the laser setup: FC, fiber coupler; HWP, half-waveplate; QWP, quarter-waveplate, GP, grating pair; PI-ISO, polarization-insensitive isolator; M1 and M2, mirrors; MM LD, multimode laser diodes.

After the single-pulse mode-locked operation was obtained in this laser, we tuned one of the wave plates while holding all the other experimental conditions unchanged. It is possible to shift the laser operation from the conventional single-pulse mode-locked operation into the NLP emission regime. This behavior was also reported by previous workers [4, 6]. We observed self-starting noise-like laser operation for a relatively large range of pumping powers. The output powers of NLPs can be varied from <0.1 W to >1.6 W. The highest pulse energy obtained was 45 nJ, with a pumping power of ~13 W. After increasing the pumping power to more than 14 W, one of the fiber couplers was damaged.

Our dispersion-mapped noise-like laser is fairly robust. We attribute this improved stability to the laser design, where NPE is accompanied by self-amplitude modulation induced by spectral filter. The role of negative GVD induced by gratings pair is also important. For the dispersion-mapped fiber laser shown in Figure 1, with a repetition rate of 31.5 MHz [14], the GVD of grating pair was set at −0.11 ps^2. This value is estimated to be slightly smaller than that of the total net positive GVD due to the fiber (~0.15 ps^2) in the cavity.

By translating the iris transversely across the laser axis (Figure 1), it is possible to modulate the central wavelength of generated pulses. We also found that the diameter of the iris determining the filter bandwidth also affects the output spectral bandwidth and duration of generated NLPs. For both narrowband and broadband NLPs, the tuning range for both cases reached 12 nm [14].

http://dx.doi.org/10.5772/61856

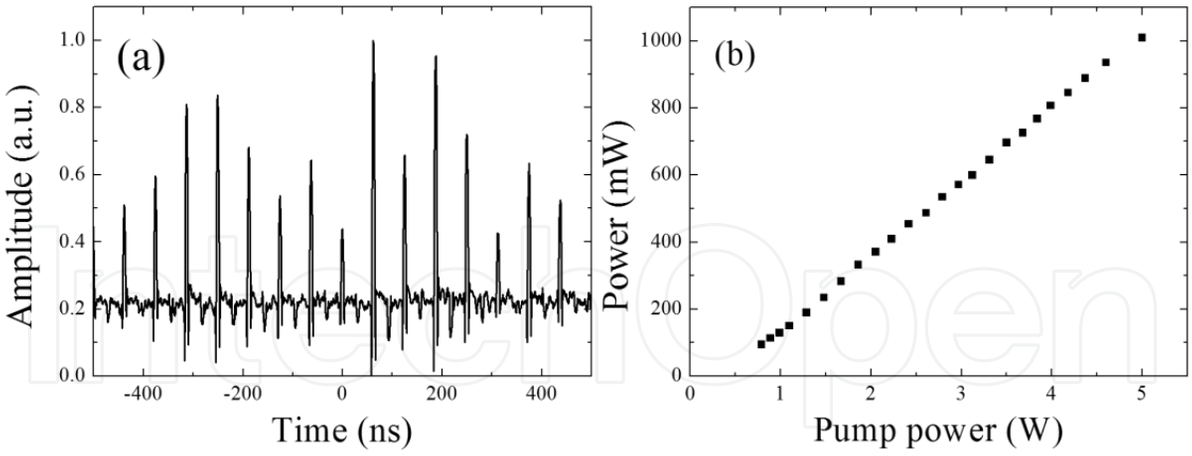

Figure 2. Oscilloscope trace of the train of noise-likes pulses (a); output power of the NLP laser vs. pumping power (b) [14].

We also set up a dispersion-mapped fiber laser in which the GVD of grating pair was set at −0.219 ps^2, while the fiber GVD was estimated to be 0.192 ps^2. Hence, the net GVD of fiber cavity became slightly negative in this configuration with a repetition rate of 15.7 MHz. The active fiber length has been increased from 1.2 m in our previous work to 7 m. Figure 2(a) shows the oscilloscope trace of the laser output as measured by a fast InGaAs detector. The behavior is typical for NLP emission state. The output powers of NLPs can be varied from <0.1 W to beyond 1 W (Figure 2(b)). The highest pulse energy obtained was ~6 nJ, with a pumping power of ~5 W. The tuning wavelength for NLP is from 1057 to 1090 nm, i.e., the tuning range is as high as 33 nm, more than twice of the previous result [14]. The spectral bandwidth of the laser output can also be varied from 6 to 54 nm. This is illustrated in Figure 3. The tuning characteristic could be important for some applications. For example, in the case of further amplification of generated pulses by fiber amplifiers, it is necessary to match the bandwidth of the oscillator with the gain spectrum of the amplifier.

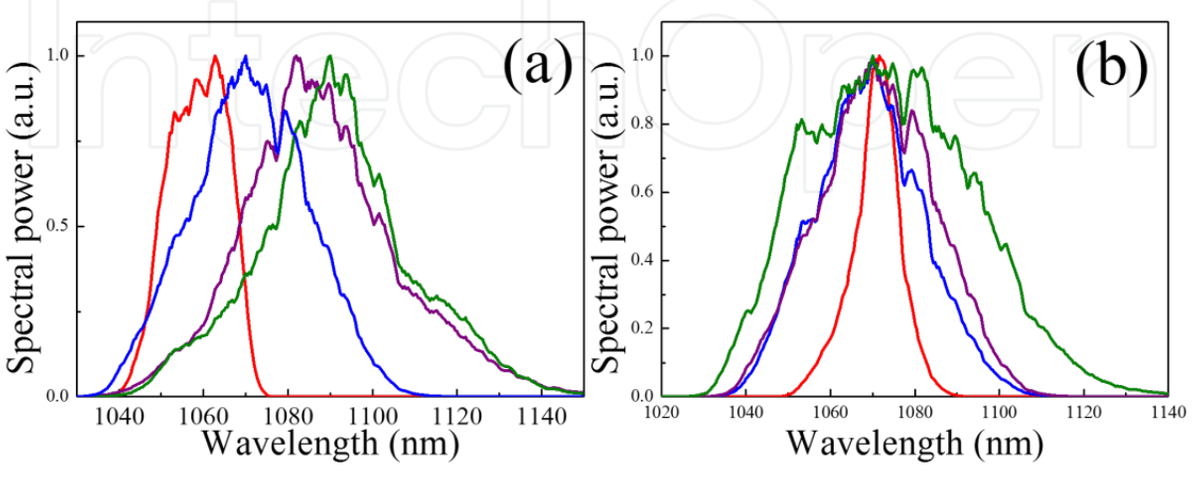

Figure 3. Optical spectra of the measured NLPs corresponding to different positions of the iris (a) and width (b).

In order to understand NLP formation, we have simulated the buildup dynamics of the laser cavity in the figure with a repetition frequency of 31.5 MHz [14]. This is performed by recognizing the cavity as consisting of several connected fiber components. Pulse propagation in each fiber section was described by the corresponding nonlinear Schrödinger coupled-mode equations [16].

$$\begin{aligned}\frac{\partial A_x}{\partial z} &= i\gamma\left\{\left|A_x\right|^2 A_x + \frac{2}{3}\left|A_y\right|^2 A_x + \frac{1}{3}A_y{}^2 A_x^*\right\} + g\left(E_{\text{pulse}}\right)A_x - \frac{i}{2}\beta_2\frac{\partial^2 A_x}{\partial t^2} \\ \frac{\partial A_y}{\partial z} &= i\gamma\left\{\left|A_y\right|^2 A_y + \frac{2}{3}\left|A_x\right|^2 A_y + \frac{1}{3}A_x{}^2 A_y^*\right\} + g\left(E_{\text{pulse}}\right)A_y - \frac{i}{2}\beta_2\frac{\partial^2 A_y}{\partial t^2}\end{aligned} \quad (1)$$

where A_x and A_y are the field envelope components; γ is the nonlinear coefficient; β_2 is the GVD; $g(E_{pulse})$ is the gain function for active fiber pieces or zero for passive fiber.

Equation (1) also includes the amplification of NLPs in active optical fibers and filtering effect due to limited gain bandwidth of the aforementioned active media. If the parameter set corresponded to the condition of minimal cavity loss for specific modes, then a stable pulse train of regular (close to Gaussian) shape will be circulated in the oscillator shortly after laser onset. A negative second-order dispersion term of ~0.02 ps^2 was assumed, neglecting high-order dispersion terms. We used Jones matrices approach to represent different polarization states as the pulses propagate through the wave plates and the PBS in our calculation. Every fiber section (active and passive) was modeled using the split-step Fourier method [16]. It was found that stable NLP waveforms began to circulate in the laser cavity after just a few round-trips (Figure 4) after pumping starts. We note further that a myriad of nonlinear effects, e.g., self-phase modulation, cross-phase modulation, four-wave mixing, etc., contribute to the generation of NLPs.

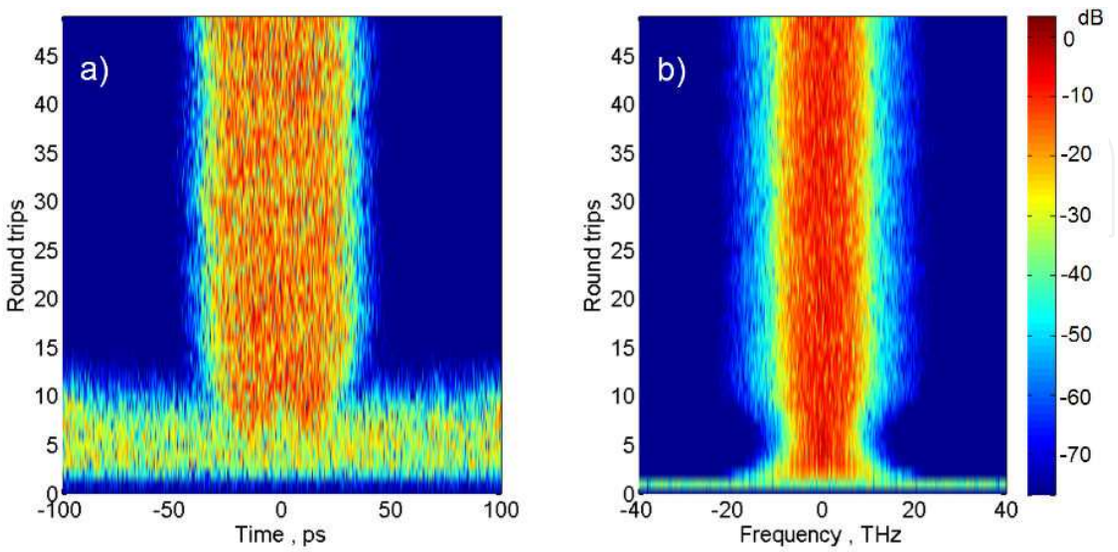

Figure 4. Building up dynamics in time (a) and spectral (b) domains of a fiber ring oscillator generating NLPs [17].

http://dx.doi.org/10.5772/61856

The simulation results for the steady state are in good agreement with experimental observations. The estimated iris filter bandwidth, corresponded iris diameter, output bandwidths, and bunch duration for the laser cavity with a repetition frequency of 31.5 MHz are listed in Table 1.

Iris diameter (mm)	Iris bandwidth (THz)	Measured output bandwidth (THz)	Calculated output bandwidth (THz)	Measured autocorrelation trace half-width (ps)	Calculated autocorrelation trace half-width (ps)
1	5	2.1	5	5	7
2	10	5.5	9	20	12
3	20	14	15	90	20

Table 1. Summary of measured and simulated results for NLPs [14].

By inserting an additional 200-m length of SMF inside the cavity (Figure 1), the repetition rate of the noise-like pulsed fiber laser was found to be reduced to ~928 kHz. The output power of the laser exceeded 1 W. Thus, the energy of the NLPs directly from the laser oscillator can be as high as 1.25 μJ (Figure 5).

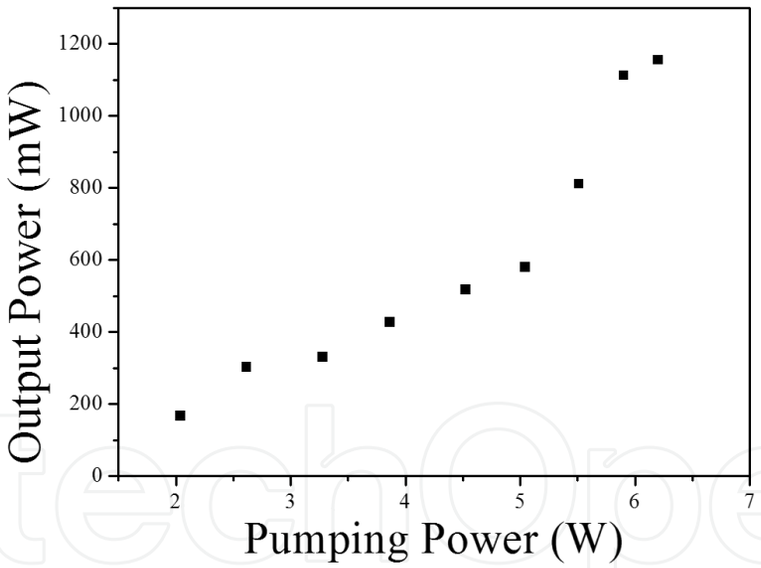

Figure 5. The pump-power dependence output of a high-energy fiber laser oscillator generating NLPs.

2.2. ANDi fiber laser

Although stable noise-like operation with controllable characteristics can be readily achieved in a dispersion-mapped fiber laser, such scheme is not practical when the required repetition rate becomes lower than 10 MHz. This is due to increased dispersion of fibers in the longer cavity and the corresponding DDL needed. Therefore, we also investigated an ANDi fiber oscillator for generation of NLPs.

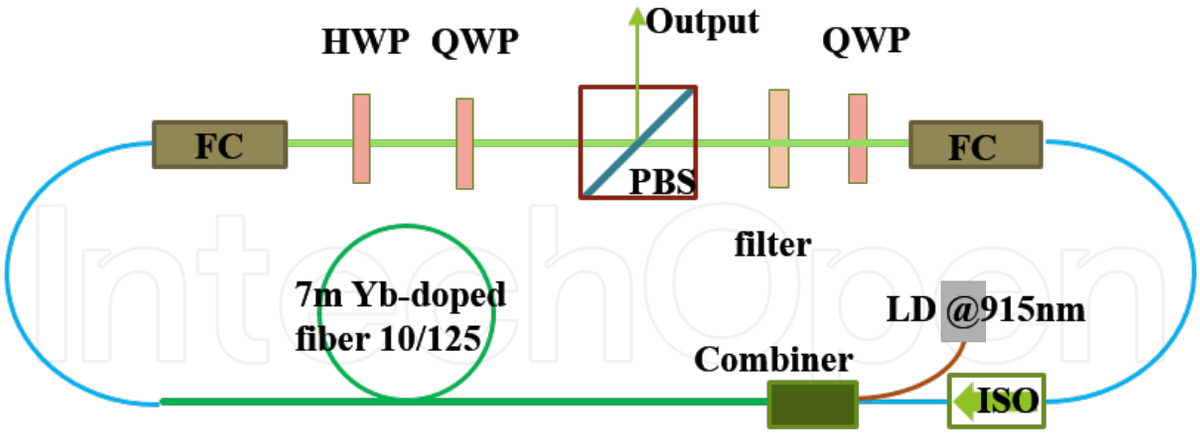

Figure 6. Schematic of ANDi fiber laser. FC, fiber coupler; HWP, half-wave plate; QWP, quarter-wave plate, PBS, polarization beam splitter; LD, laser diode; ISO, isolator.

The ANDi laser is perhaps one of the simplest designs of mode-locked Yb-doped fiber oscillators. There is no need for dispersion-compensation components such as the grating pair [18]. Typically, the dispersion in the cavity of an ANDi laser is managed by a narrow-bandwidth interference filter. We found that after proper alignment of the waveplates, an ANDi laser can also generate NLPs. In comparison with the dispersion-mapped laser, the achievable pulse energy at the output is larger. An average power of 850 mW (pumped at 2 W) at a repetition rate of ~15 MHz, which corresponds to pulse energy of 55 nJ, was obtained for a cavity length of 13 m. The bandwidth of generated NLP was as high as 21.8 nm. When the cavity length was increased to 62.5 m or a laser repetition rate of 3.2 MHz, the spectral bandwidth approaches a value at least fourfold higher than the regular mode-locked pulse. The central wavelength of the laser is 1096 nm and the spectral bandwidth can reach 83 nm. The laser can also deliver an average output power of 400 mW (pumped at 1 W) or a pulse energy of 125 nJ.

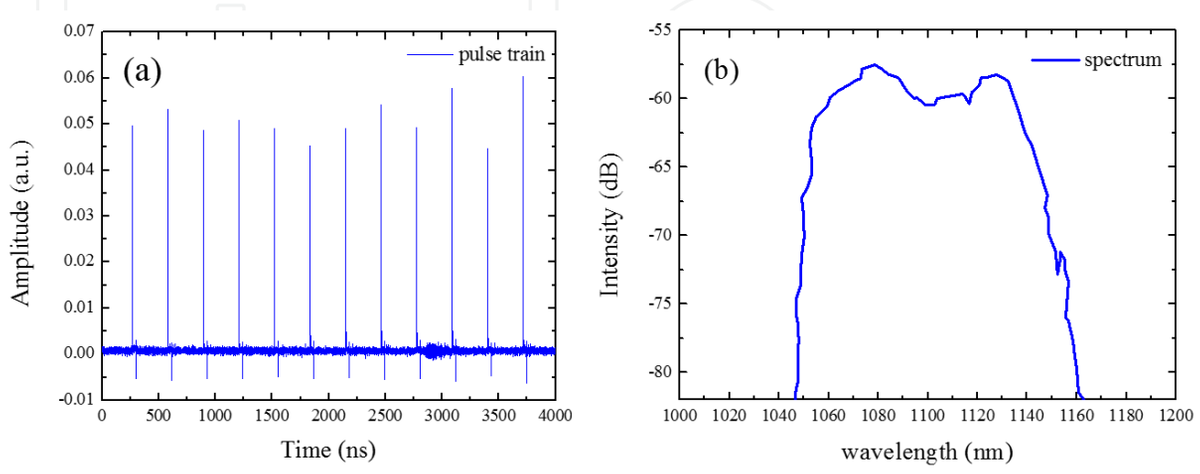

Figure 7. Characteristic of ANDi laser. (a) Pulse train and (b) optical spectrum.

http://dx.doi.org/10.5772/61856

In summary, using cladding-pumped Yb-doped active fibers and high-power multimode laser diodes, we demonstrated that NLPs with relatively high energies can be generated with either dispersion-mapped or ANDi cavities. The latter exhibits some advantages over the former, e.g., ease of alignment, lower threshold, and higher pulse energy. The achieved average power of NLPs can be as high as ~1 W and, limited only by damage threshold of available fiber couplers. On the other hand, it is possible to control temporal and spectral characteristics of NLPs generated by the dispersion-mapped laser over a broad range. This is not possible for the ANDi laser.

3. SC generation by NLPs

In the past decade, tremendous progress has been made in SC generation (SCG) [19]. Nowadays, SC source has been widely used in many applications such as OCT, frequency metrology, and wavelength division multiplexing systems [20–22]. Using rare-earth-doped fiber lasers, especially Yb-doped fiber lasers operating at a high power with a short pulse width as the pump laser, the spectral bandwidth and the output power of SC sources have increased dramatically [23–25].

The nonlinear mediums used for SCG have also evolved from bulk media [25, 26] to conventional optical fibers [27], and then PCFs [28–32] for visible light, near-infrared, and mid-infrared SCG. The SC generated with PCFs is popular due to the controllable ZDWs and high nonlinearity [19]. Moreover, very powerful light sources at ~800 nm and ~1 μm can be used for efficient SC pumping. However, PCFs are still expensive and not widely available. Furthermore, especially for high-power operations, splicing between PCF and pigtailed fiber pump source is a significant challenge because of mode field mismatch and the microhole collapse effect [33]. Standard SMFs for optical communication, on the other hand, are inexpensive and easy to integrate. Pumping standard SMF at ~800 nm or ~1 μm, however, is not so efficient because these popular pump wavelengths are located in the normal dispersion region of the SMF. It requires much more pump power to excite SC compared with SCG in the anomalous regime. Further, in the case of CW or picosecond duration pump sources, the SC spectrum so generated exhibits very strong oscillations [34]. Recently, it has been demonstrated that such spectral oscillations can be explained by cascaded Raman scattering [34–36]. Such modulations in spectrum are not desirable for applications such as OCT.

On the other hand, more broadband pumps have been shown to result in SC with a smoother spectrum [37]. As reported by Horowitz *et al.* [9], NLPs can be successfully used for such a purpose. Besides a very large optical bandwidth, NLPs are capable of propagating without distortion through a lengthy dispersive medium over a long distance [9]. Later, Hernandez-Garcia *et al.* [38] demonstrated flat broadband SCG by pumping SMF in the anomalous dispersion region with a train of NLP at the central wavelength of 1.5 μm. The energy threshold was as low as ~12 nJ. Recently [39], we have reported similar desirable characteristics (a low threshold and a flat spectrum) by pumping SMF in the normal dispersion regime with NLPs. In contrast to the anomalous case, the physical mechanism of such SCG is cascaded Raman

scattering that results in significant spectral broadening in the longer wavelength regions of the SC whereas the Kerr effect is responsible for smoothing the spectrum of generated SC.

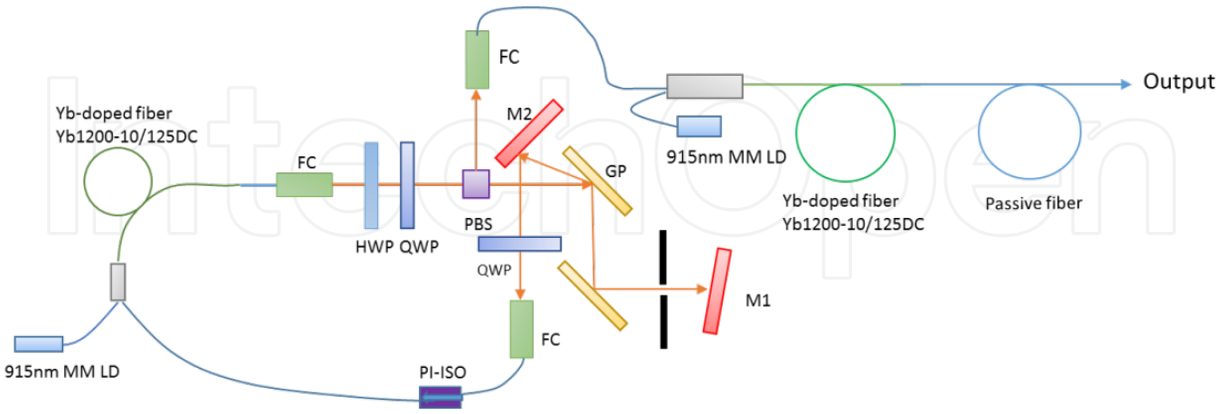

Figure 8. Schematic of the experimental setup: FC, fiber coupler; HWP, half-wave plate; QWP, quarter-wave plate; GP, grating pair; PI-ISO, polarization-insensitive isolator; ISO, Faraday isolator; M1 and M2, mirrors; MM LD, multi-mode laser diodes.

The experimental setup for SCG is shown in Figure 8. The pump source is a dispersion-mapped Yb-doped fiber laser based on the ring cavity design that can generate tunable NLPs with energies as high as ~45 nJ with a central wavelength of ~1 μm [14]. This laser can also be configured to generate stable mode-locked femtosecond pulses. The use of negative dispersion delay line and the spatial spectral filter (Figure 8) was found to be important for such a high-power noise-like operation. In the NLP regime and when pumped at ~7 W, the oscillator irradiates a pulse train with a repetition rate of ~31.5 MHz, an average power of ~600 mW, and an average noise-like bunch duration of ~45 ps. Typical spectrum and intensity autocorrelation trace of the NLP laser are shown in Figure 9. The spectral bandwidth of the NLPs was ~10 nm full width at half maximum (FWHM). We also simulated the buildup dynamics of our laser cavity by recognizing it as consisting of several connected fiber components. Assuming a thermal Gaussian noise as a source of oscillations, we found the conditions where repeated NLPs begin to circulate in the laser cavity after hundreds of round-trips. Such simulations yield results (spectra, autocorrelation traces) that are close to experimental measurements [39]. An example of simulated NLP characteristics is shown in Figure 10.

The NLPs from the seed laser described above were boosted up to an average power of ~2 W in a single 1.2 m-length Yb-doped amplifier stage and used as a pump to excite the SC. Several different SMFs were investigated for SCG. They were spliced to the output fiber end of the amplifier. All fibers are single mode at the pump wavelength (~1 μm). They were selected to examine the effects of nonlinearity on SCG. The parameters of the fiber investigated are summarized in Table 2. The dispersion coefficients β_n at 1060 nm central wavelength and the ZDW for F1060c were calculated from the Sellmeier equation for 5% GeO_2 doped silica [40]. For SMF980A and UHNA3 fibers, the parameters β_n and ZDW were calculated from dispersion curves provided by fiber manufactures.

http://dx.doi.org/10.5772/61856

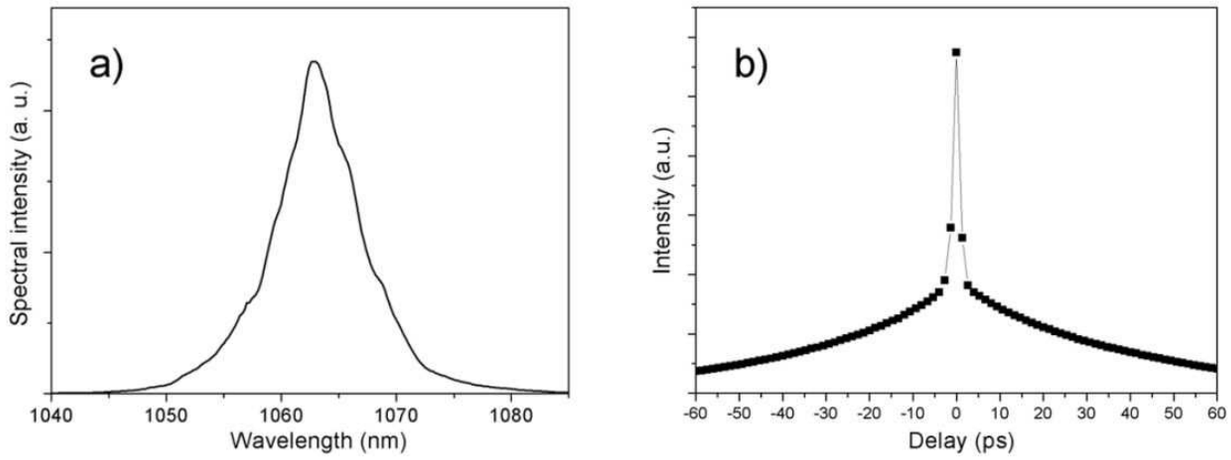

Figure 9. The experimentally measured spectrum (a) and intensity autocorrelation trace (b) of NLPs irradiated by the oscillator in Figure 1.

Fiber Type	F1060c (Lightwave Tech)	SMF980A (POFC, Taiwan)	UHNA3 (Nufern)
Mode-field diameter at 1060 nm	8.4 μm	4.5 μm	2.6 μm
Numerical aperture	0.11	0.21	0.35
Core GeO_2 concentration[1]	~3 mol.%	~10 mol.%	~20 mol.%
Zero-dispersion wavelength	1330 nm	1570 nm	1900 nm
Nonlinear coefficient at 1060 nm[2]	3.2 W^{-1} km^{-1}	13.7 W^{-1} km^{-1}	52.3 W^{-1} km^{-1}
Dispersion coefficients at 1060 nm[3]	$\beta_2 = 19.0\times10^{-3}$ ps^2/m, $\beta_3 = 4.5\times10^{-5}$ ps^3/m, $\beta_4 = -5.991\times10^{-8}$ ps^4/m, $\beta_5 = 1.879\times10^{-10}$ ps^5/m, $\beta_6 = -6.890\times10^{-13}$ ps^6/m	$\beta_2 = 28.1\times10^{-3}$ ps^2/m, $\beta_3 = 2.154\times10^{-5}$ ps^3/m, $\beta_4 = 8.187\times10^{-8}$ ps^4/m, $\beta_5 = 7.351\times10^{-11}$ ps^5/m, $\beta_6 = -3.965\times10^{-13}$ ps^6/m	$\beta_2 = 58.9\times10^{-3}$ ps^2/m, $\beta_3 = 2.32\times10^{-5}$ ps^3/m, $\beta_4 = 1.04\times10^{-7}$ ps^4/m, $\beta_5 = 2.078\times10^{-10}$ ps^5/m, $\beta_6 = -5.241\times10^{-13}$ ps^6/m
Spool length	50 m	50 m	10 m
Splicing loss	~0.5 dB	~1.5 dB	~3 dB

[1]Estimated data;

[2]Estimated from Eq. (2) assuming n_2=3×10^{-20}m^2/W for F1060c; n_2=3.7×10^{-20}m^2/W for SMF980A; n_2=4.7×10^{-20}m^2/W for UHNA3, respectively;

[3]For F1060c, fibers were calculated from Sellmeier equation for 5% GeO_2 doped silica [41]; for SMF980A and UHNA3, fibers were calculated from dispersion curves provided by fiber manufactures.

Table 2. Fiber parameter and characteristics.

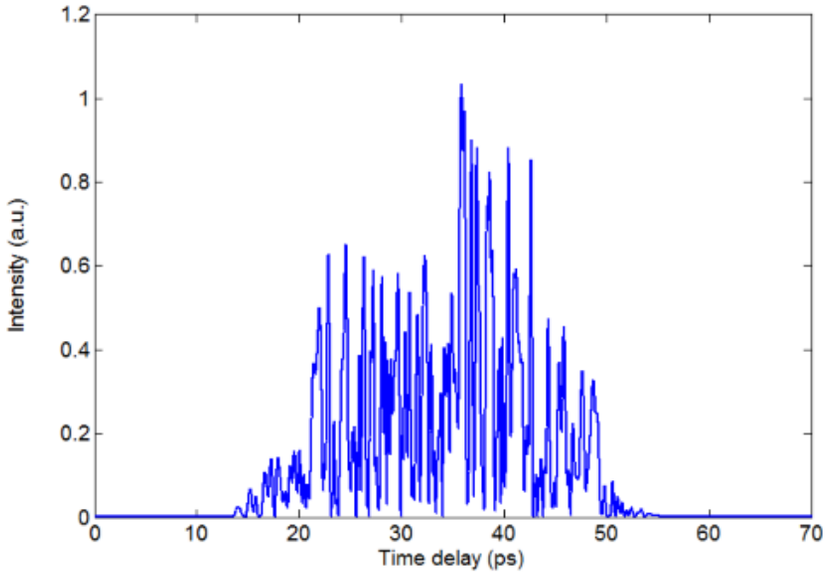

Figure 10. An example of simulated NLP waveforms.

3.1. Theoretical analysis and numerical simulation results for SCG

SC generation in an SMF by pumping with NLPs is analyzed by solving the general nonlinear Schrödinger equation in the frequency domain [19] as follows:

$$\frac{\partial A'(z,\omega)}{\partial z} = i\frac{\gamma\omega}{\omega_0}\exp\{-L(\omega)z\}F\left\{A(z,T)\int_{-\infty}^{\infty}R(T')\left|A(z,T-T')\right|^2 dT'\right\}, \tag{2}$$

where A and A' represent the electric field envelopes and γ is the nonlinear coefficient [16].

$$\gamma = \frac{2\pi n_2}{\lambda_0 A_{eff}} = \frac{8n_2}{\lambda_0 d^2}, \tag{3}$$

wherein n_2 is the nonlinear refractive index and d is the mode-field diameter. F{} denotes the Fourier transform and $R(t)$ is the full nonlinear response function, which includes instantaneous (Kerr) and delayed (Raman) terms and can be modeled by a single damped harmonic oscillator [16].

$$R(t) = (1-f_R)\delta(t) + f_R\frac{\tau_1^2+\tau_2^2}{\tau_1\tau_2^2}\exp\left(-\frac{t}{\tau_2}\right)\sin\left(\frac{t}{\tau_1}\right)\Theta(t), \tag{4}$$

where f_R = 0.18 is the fractional contribution of the delayed Raman response, τ_1 is the time constant related to the phonon frequency, and τ_2 is the time constant related to the damping of the phonons. $\Theta(t)$ is the Heaviside step function and $\delta(t)$ is the Dirac delta function. From the Raman gain spectra, it is well known [35, 41, 42] that silica glass and Germanate glass have very similar phonon frequencies but very different phonon damping times. These time constants are listed in Table 3.

http://dx.doi.org/10.5772/61856

Absorption in fiber was neglected. In Eq. (2), $L(\omega)$ is the linear operator representing dispersion of the SMF, given by $L(\omega) = i(\beta(\omega)-\beta(\omega_0)-\beta_1(\omega_0)(\omega-\omega_0))$, where β_1 is the first-order dispersion coefficient associated with the Taylor series expansion of the propagation constant β about ω_0. Up to six high-order dispersion terms were taken into account for simulations (Table 2).The non-linear coefficient γ was calculated using Eq. (3) at a central wavelength of ~1.06 μm and using mode-field diameters of fibers according to Table 1. The nonlinear refractive index for fibers were assumed to be 3×10^{-20} m^2/W, 3.7×10^{-20} m^2/W, and 4.7×10^{-20} m^2/W for F1060c, SMF980A, and UHNA3, respectively, according to Eq. (6) in Ref. [43]. Finally, the fourth-order Runge-Kutta algorithm was used to solve Eq. (2). The simulation results for the three different fiber samples (according to Table 2) are presented in Figures 11–19. For each fiber sample, we simulated the evolution of three different types of pulses of equal energy propagating through the fiber. The pulse energy in every case corresponded to the experimental conditions including splicing loss (Table 2). The first input waveform used in these calculations was a simulated NLP (Figure 10), of which characteristics (duration and bandwidth) corresponded to that of our NLP laser (Figure 9). The second input pulse waveform was that of a mode-locked Gaussian pulse with a duration of 45 ps, which is similar to the duration of our NLPs (Figures 9 and 10). The third input waveform was that of a mode-locked Gaussian pulse with a duration of 200 fs. Its spectral bandwidth (~5 THz) is similar to the bandwidth of our NLP (Figure 9).

Fiber type	**F1060c (Lightwave Tech), SMF980A (POFC, Taiwan)**	**UHNA3 (Nufern)**
τ_1	12.2 fs [42]	12 fs [35, 41]
τ_2	32 fs [42]	83 fs [35, 41]

Table 3. Single damped harmonic oscillator fitting constants.

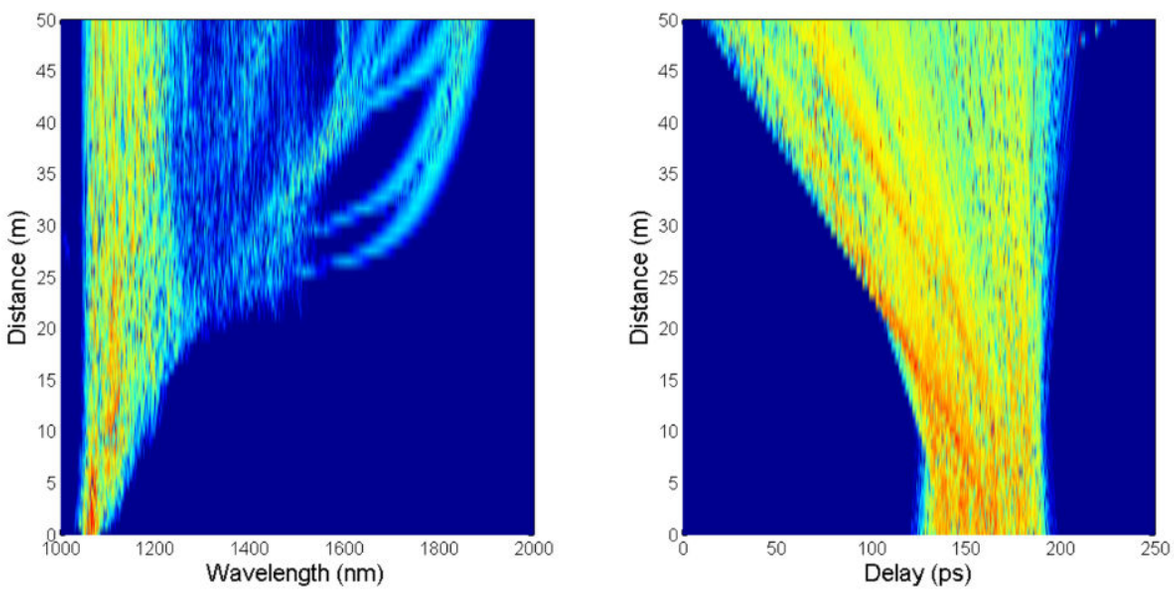

Figure 11. SC evolution in a 50-m piece of F1060c fiber pumped by NLP with 90-nJ pulse energy.

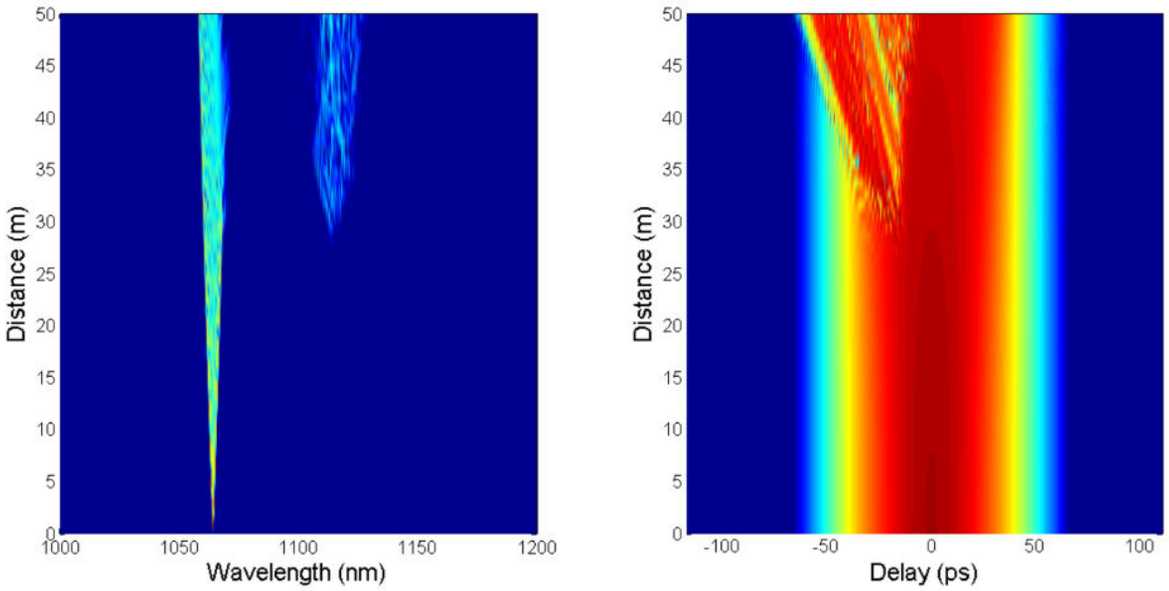

Figure 12. SC evolution in a 50-m piece of F1060c fiber pumped by Gaussian pulse with 45-ps duration and 2-kW peak power.

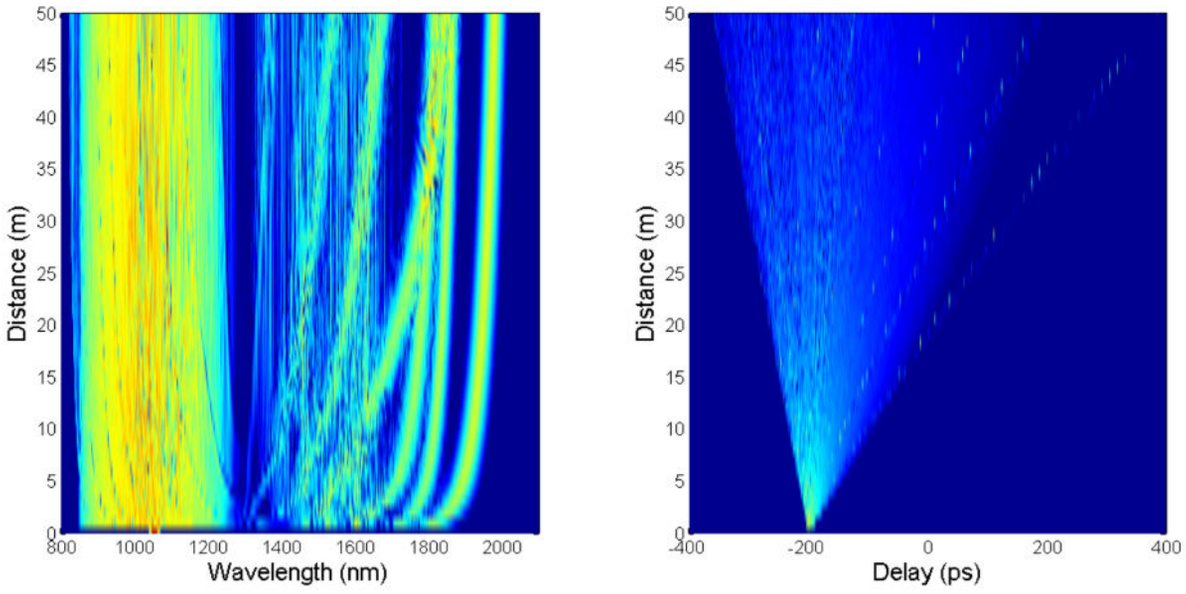

Figure 13. SC evolution in a 50-m piece of F1060c fiber pumped by Gaussian pulse with 200-fs duration and 350-kW peak power.

Examining the simulation results (Figures 11–19), we find that SC evolution in the case of NLP pumping is different from those of mode-locked picosecond or femtosecond Gaussian pulses for the three fiber samples we studied. Note that picosecond Gaussian pulses (~ 45 ps) can only generate from one to three clear Raman peaks in its spectrum (Figures 12, 15, and 18). That situation is explained by cascaded Raman scattering and is typical for narrowband pumping

http://dx.doi.org/10.5772/61856

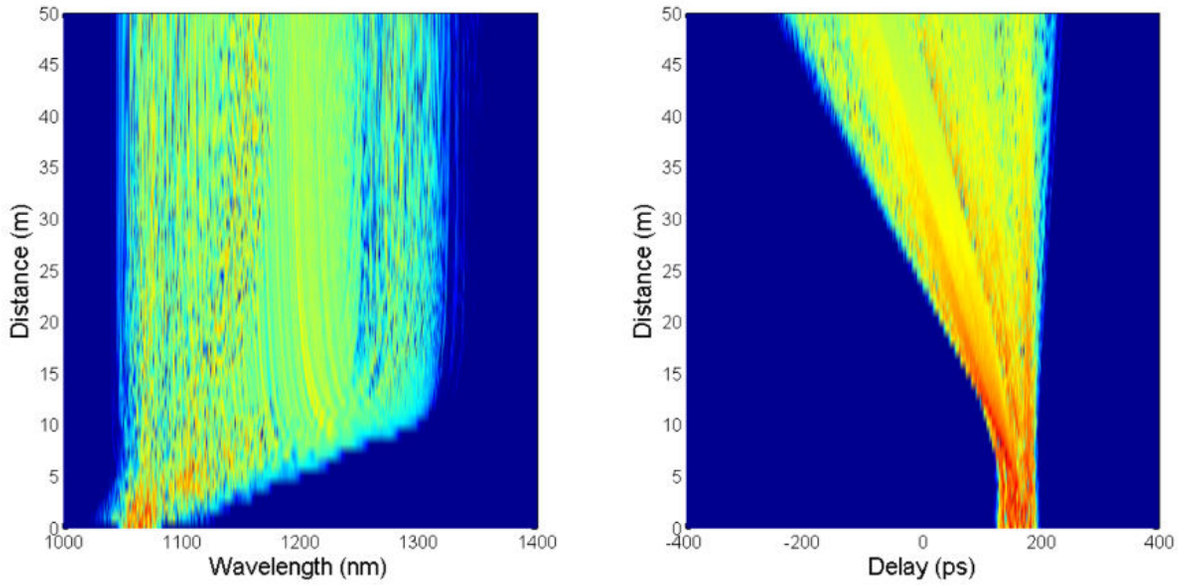

Figure 14. SC evolution in a 50-m piece of SMF980A fiber pumped by NLP with 45-nJ pulse energy.

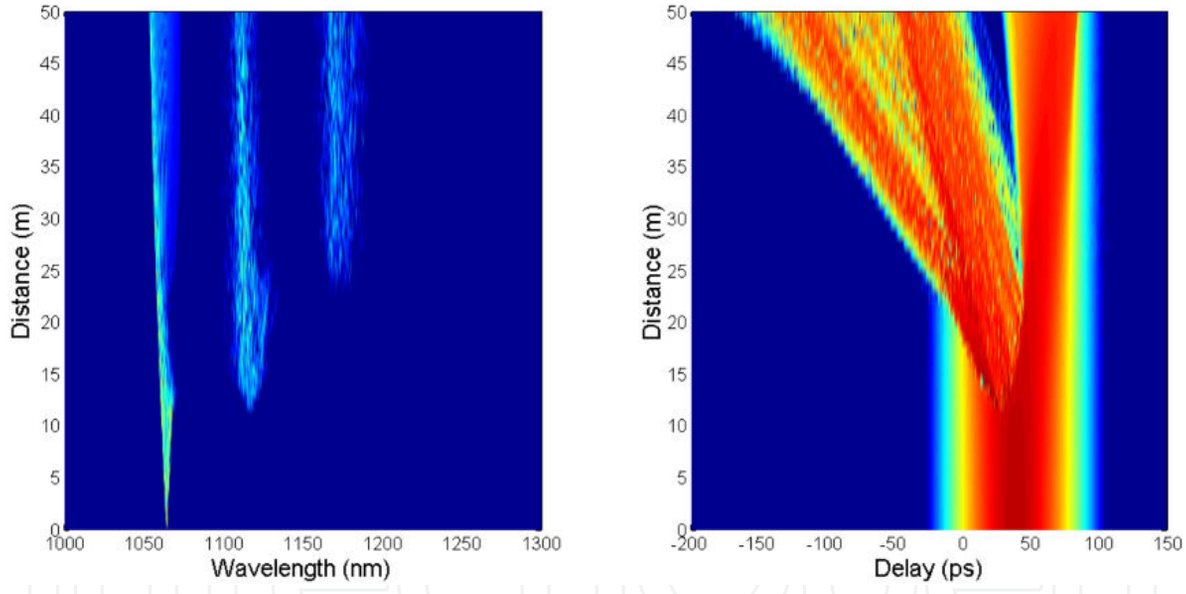

Figure 15. SC evolution in a 50-m piece of SMF980A fiber pumped by Gaussian pulse with 45-ps duration and 1-kW peak power.

with moderate powers in the normal-dispersion region [32–35, 44]. As for the shorter mode-locked Gaussian pump pulse (200 fs), it can generate broadband SC (Figures 13, 16, and 19) of which the behavior is dependent on relative positions of pump central wavelength and the ZDW. In the case when spectral difference between them is small, e.g., in the case of the F1060c fiber, initial spectral broadening caused by self-phase and cross-phase modulations is sufficient for the spectrum to approach the ZDW (Figure 13). Then, further spectral evolution is described by soliton fission, which is typical for SCG by ultra-short pulse [19]. We should

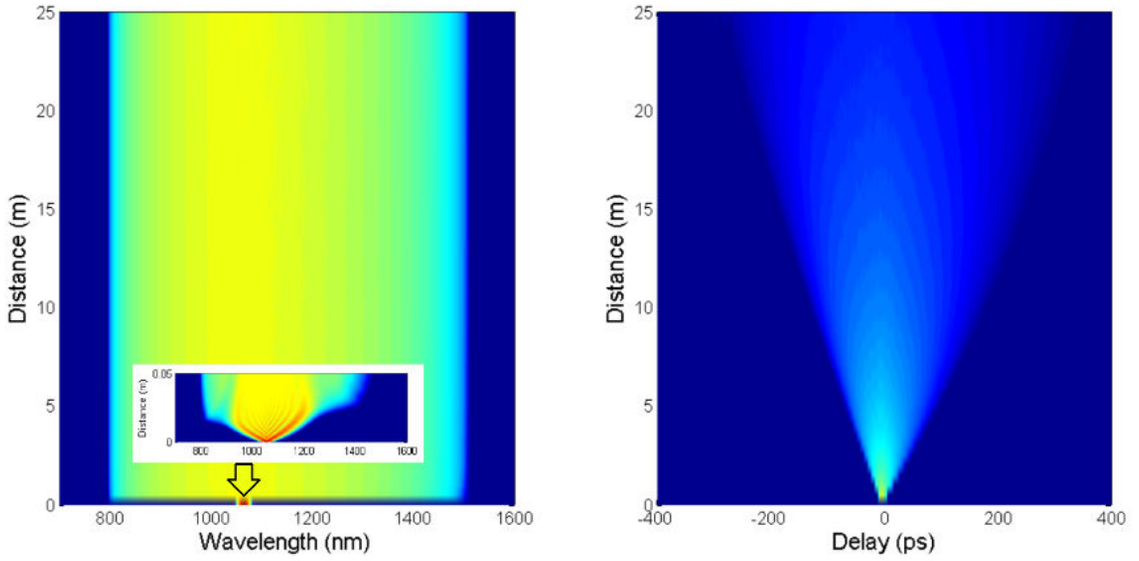

Figure 16. SC evolution in a 50-m piece of SMF980A fiber pumped by Gaussian pulse with 200-fs duration and 200-kW peak power.

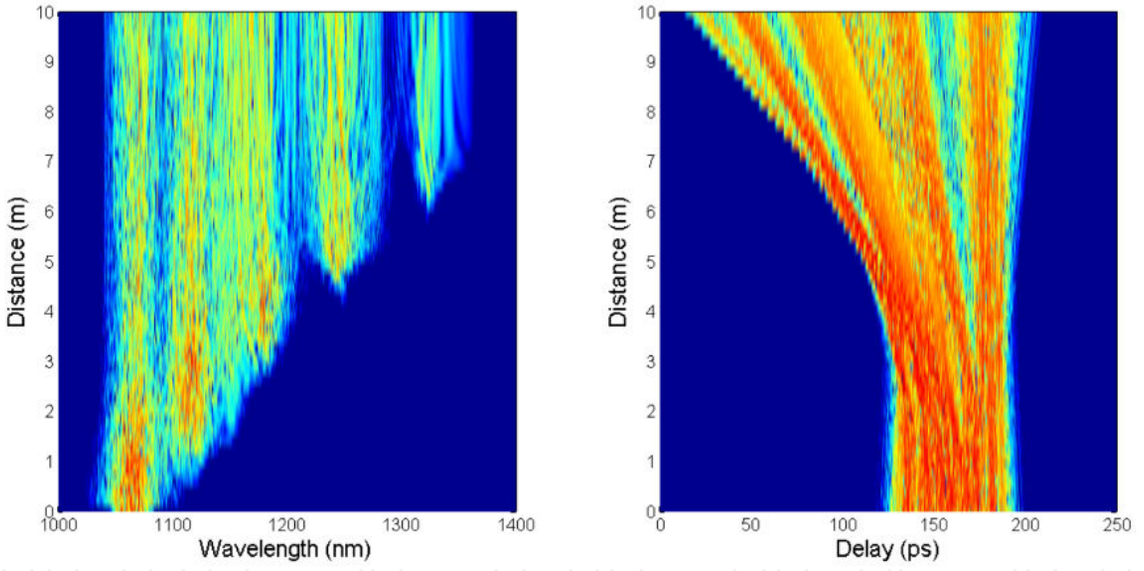

Figure 17. SC evolution in a 10-m piece of UHNA3 fiber pumped by NLP with 21-nJ pulse energy.

mention that efficient femtosecond pulse pumping requires significant peak power (hundreds of kWs) especially in the cases when ZDW is shifted to the longer wavelength region. Our simulations show that, for SMF980A and UHNA3 fibers, where the ZDWs are equal 1570 and 1900 nm, respectively, we may not be able to extend the SC to the anomalous dispersion region (Figures 16–19). Also, 200-fs-wide Gaussian pump pulses excite SC in first tens of centimeters of the SMF (see inset in Figures 16–19). Afterwards, its spectrum does not change.

It is interesting to note that NLPs, in comparison to mode-locked Gaussian pulses of similar waveform durations, exhibit the spectral broadening mainly in the longer wavelength (relative

http://dx.doi.org/10.5772/61856

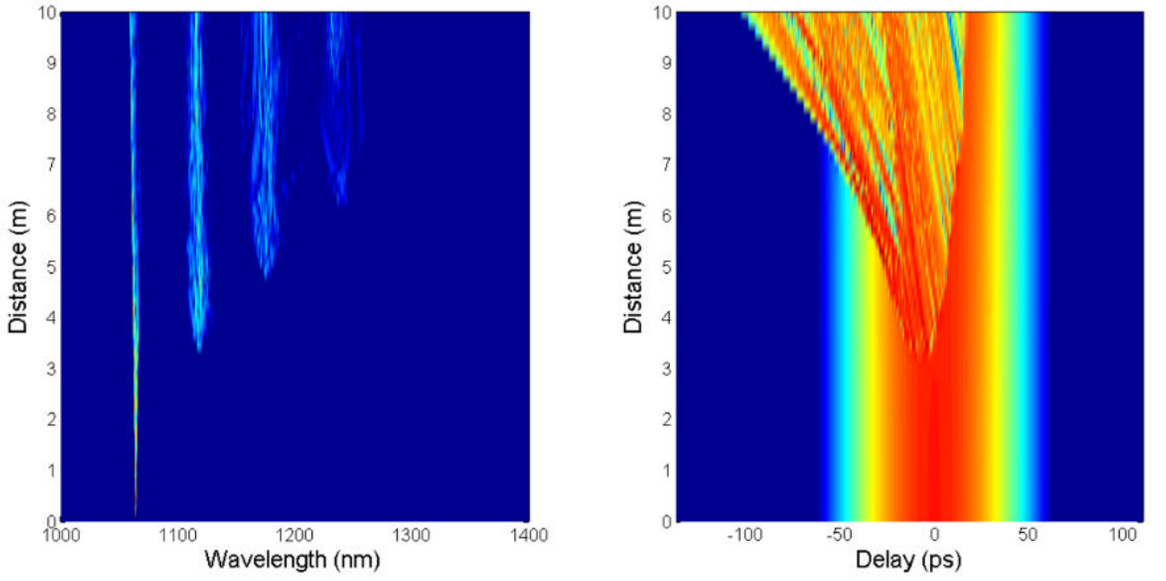

Figure 18. SC evolution in a 10-m piece of UHNA3 fiber pumped by Gaussian pulse with 45-ps duration and 450-W peak power.

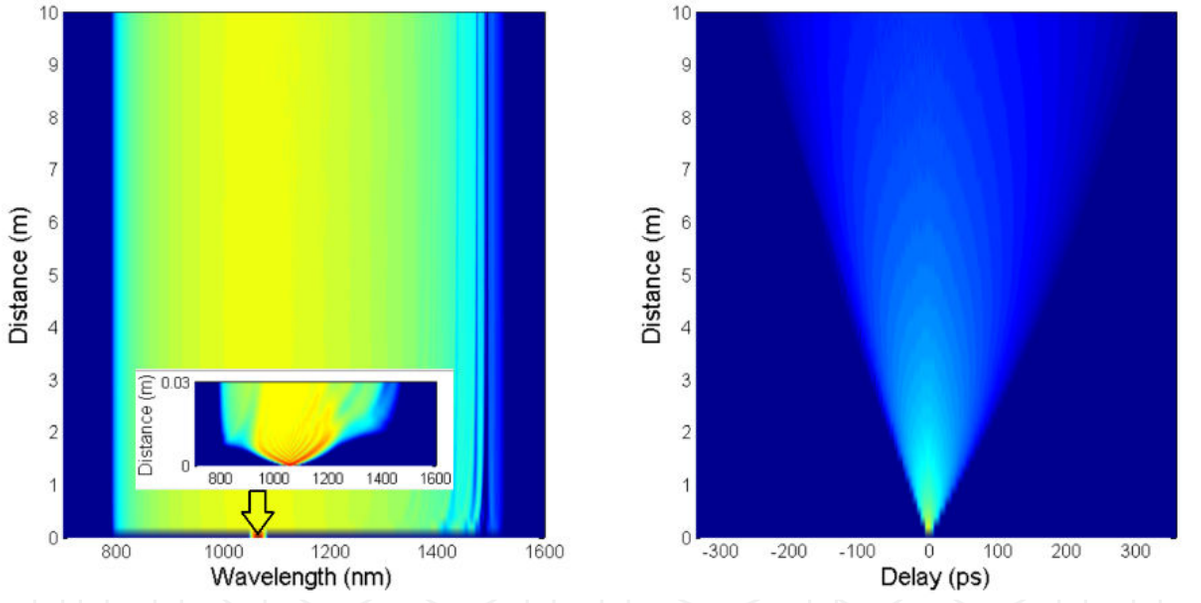

Figure 19. SC evolution in a 10-m piece of UHNA3 fiber pumped by Gaussian pulse with 200-fs duration and 100-kW peak power.

to the pump wavelength) region (Figures 11, 14, and 17). In the case of the UHNA3 fiber, the distinctive Raman orders can be found in SCG evolution spectrum (Figure 17). The broader Stokes lines and much smoother SC spectrum can be explained by broadband pumping [37], which is the feature of NLP [19]. For the two other fibers (F1060c and SMF980A), simulations suggest that even smoother SC spectra are expected to be generated. This may result from reduced Germanium concentration of their fiber core compared with that of the UHNA3 fiber.

That results in reduced phonon damping times (Table 3) and the suppression of the contribution of the Raman term in the full nonlinear response function (Eq. (4)). It is notable that pulse energy of our NLP, ~90 nJ, is sufficient to generate SC that approaches the ZDW in the case of the F1060c fiber (Figure 11). In comparison, a mode-locked pulse of a similar duration and energy can generate only one Stokes line (Figure 12). To reach a similar SC bandwidth, however, the evolution of NLP-excited SC takes longer distance in the fiber.

Recently, it has been theoretically predicted that Raman-induced spectral shift, which may happen in the normal dispersion region, is responsible for asymmetry of spectral broadening [45]. The distinctive Raman orders in Figures 12, 15, and 18 for MLPs suggested that multiple Raman processes, i.e., cascaded Raman scattering, could be responsible for initial spectral broadening for NLP pumped SMF. Therefore, we have tentatively attributed our calculated behavior of the broadband SC emission to Raman amplification of noise in the SMF [19]. Later on, after the SC spectrum approaching ZDW, further SCG process becomes soliton fission like.

First, we spliced F1060c fiber directly to the output of amplifier. Since the mode-field diameters of spliced fibers were not too much different, the splice loss was low (<0.5 dB). We measured a series of SCG spectra with the F1060c pumped at different powers (Figure 20(a)). The simulated SCG spectrum at an input power of 1500 mW in Figure 20(b) agrees quite well with our experimental observations.

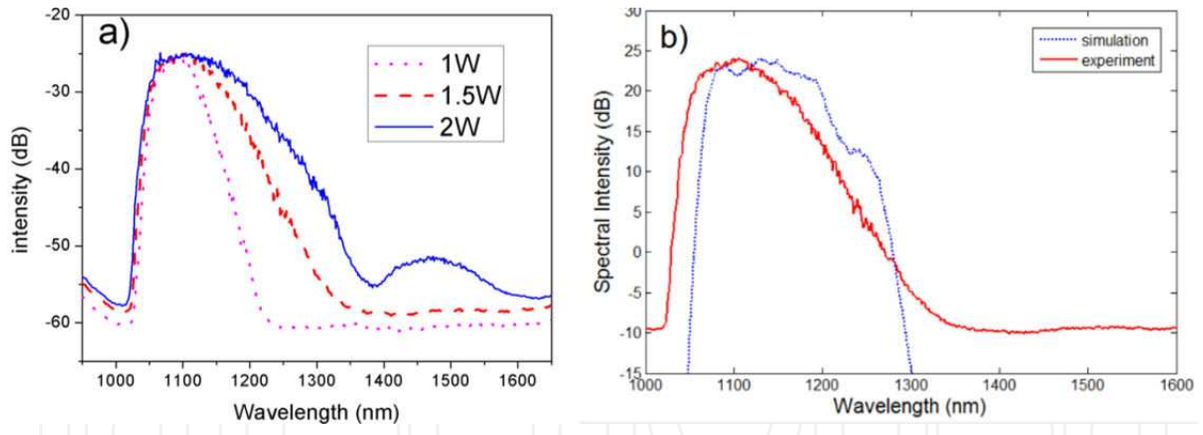

Figure 20. (a) The experimental spectra of SCG in F1060c fiber at different input powers. (b) The comparison between experimental and simulated spectra of SCG in F1060c fiber at 1500-mW input power.

Then, we examined SCG in the SMF980A fiber, which has smaller core diameter (Table 2). Owing to a large difference in mode areas, we used a short piece (~20 cm) of Newport F-SV fiber in between the connecting fibers. Hence, the total splice loss between the active fiber in the amplifier and SMF980A was ~1.5 dB. Similar to the previous case, we measured a series of SCG spectra at different pump powers (Figure 21(a)). The simulated SCG spectrum at an input power of 1600 mW (Figure 21(b)) again shows good agreement with experimental measurement. These two simulations and experimental results (for F1060c and SMF980A fibers) indicate smooth spectra of SC generated this way.

http://dx.doi.org/10.5772/61856

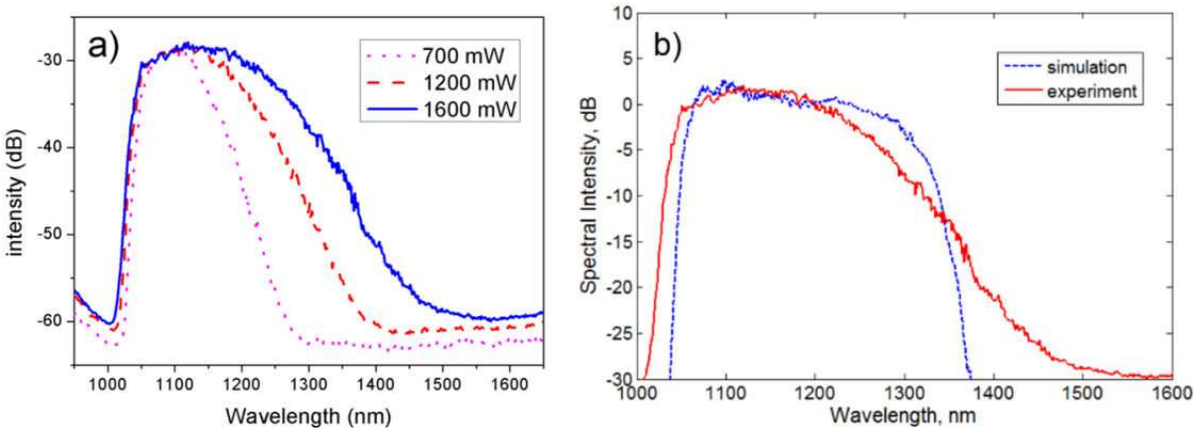

Figure 21. (a) The experimental spectra of SCG in SMF980A fiber at different input powers. (b) The comparison between experimental and simulated spectra of SCG in SMF980A fiber at 1600 mW input power.

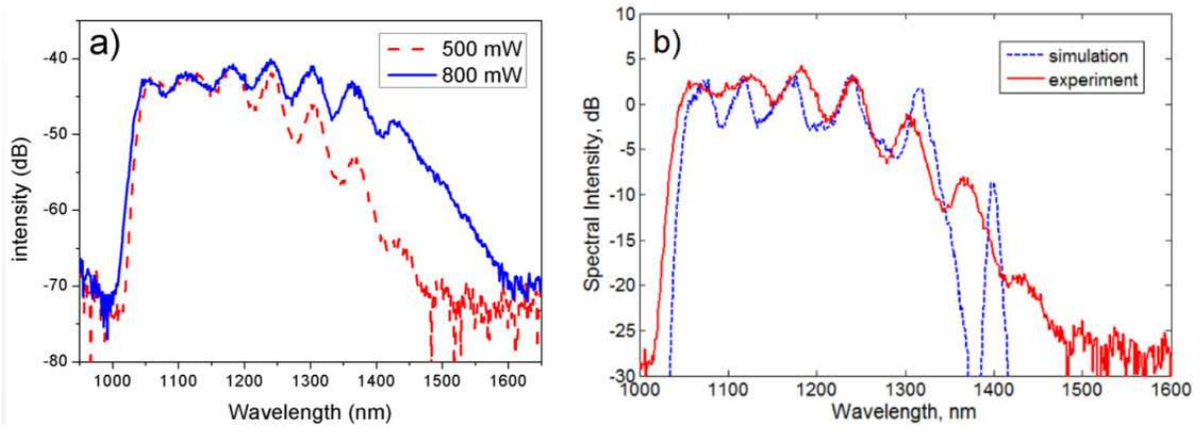

Figure 22. (a) The experimental spectra of SCG in UHNA3 fiber at different input powers. (b) The comparison between experimental and simulated spectra of SCG in UHNA3 fiber at 500 mW input power.

We also studied SCG by the UHNA3 fiber using our NLPs. The total splice loss was ~3 dB. The spectra of SCG generated in this fiber at different input powers are plotted in Figure 22(a). Spectral oscillators and broadened bandwidth in the SCG spectrum are evident and in good agreement with the simulated results (Figure 22(b)).

Examining Figures 20-22, we find that SCG spectra are different for the three types of fiber used and pumping conditions. Obviously, in order to get larger spectral broadening using SMFs with relatively small nonlinear coefficients, relatively longer fiber length is required (50 m for F1060c and SMF980A). Herein, the fiber with a larger nonlinear coefficient provides more broadband response (~260 nm vs. ~160 nm width at −10 dB level and ~1.5 W input power for SMF980A and F1060c, respectively) (Figures 20(a) and 21(a)). Applying UHNA3 fiber with high nonlinearity (γ = 52.3 W^{-1} km^{-1}) allows achieving significant spectral broadening (~440 nm at −10 dB level) with a shortened fiber length (10 m) and reduced input average power (~800 mW) of NLP. But we should mention that the shape of SCG spectra (Figure 22(a))

becomes modulated. The simulation results also indicate such behavior related with cascaded Raman scattering. We believe that such behavior can be explained by significantly increased doping concentration of germanium in UHNA3 fiber (~20 mol.%). This results not only in nonlinearity enhancement [45] but also in modification of Raman response function [43]. It is known that Raman gain in Germatate glass is much stronger than that in silica glass. As a result, the damping time of delayed Raman response in highly doped germanium fiber is longer (Table 3), which causes spectral oscillations.

In summary, we have reported a study of SCG with a scheme that uses a SMF pumped in the normal dispersion regime (~1 μm) by NLPs from a dispersion-mapped fiber laser. We showed SCG results using different SMFs and demonstrated that using a higher doping concentration of Germanium (~20 mol.%) in SMF results in the enhancement of optical fiber nonlinearity, reducing SCG threshold, and change in the Raman response function. The last one is found to be responsible for the appearance of oscillations in the SC spectrum. The achieved SC exhibits low threshold (21 nJ) and a broadband spectrum over 1030–1470 nm with a relatively short fiber length (10 m).

We believe that the achieved low energy threshold and flat SC spectrum are caused by unique properties of NLP (broadband spectral range and ability to propagate over a long distance). Higher level of spectral oscillation is caused by higher Raman gain in germanium doped fiber, which results in increasing the damping time of Raman response function.

Naturally, it is possible to use NLPs from the ANDi laser for SCG. Examples of such studies will be described in Sec. 4 of this chapter.

4. Applications for OCT

OCT is a technique of optical imaging that is extensively used in biomedical and clinical studies. The first OCT images were demonstrated by Huang *et al.* [46]. The authors confirmed that OCT is superior for obtaining images in highly scattering media. In 1993, the first *in vivo* OCT images were obtained by Fercher [47] and Swanson [48]. Thereafter, OCT technology advanced rapidly and was readily accepted for use in ophthalmology. In 1996, the first commercial ophthalmic OCT instrument by Carl Zeiss Meditec made its appearance [49]. Another significant milestone is the spectral-domain interferometric technique proposed theoretically in 1995 by Fercher *et al.* [50]. Soon afterwards, Wojtkowski showed that the technique was workable by imaging the retina [51]. Comparative studies of TD-OCT and SD-OCT were first reported by De Boer [52] and Leitgeb [53].

OCTs typically employ near-infrared light in order to achieve deep penetration in biological samples or scattering media. The axial resolution of an OCT is determined by the width of the field autocorrelation function, or the inverse of the spectral bandwidth of the light source. Thus, a broadband light source is required for ultra-high-resolution OCT.

Superluminescent diode (SLD), amplified spontaneous emission (ASE), and SC sources have been widely used as the light source for OCT systems. OCTs with SLDs typically have an axial

resolution of 10–15 μm, due to the limited gain bandwidth (~100 nm or less). The bandwidth of ASE sources is also around several tens of nanometers. Thus, ultra-high-resolution OCT typically employs SC sources. In 2001, Hartl *et al.* reported the first OCT system based on SC generated with a PCF pumped by a femtosecond Ti: sapphire laser [54]. They achieved an axial resolution of ~2.5 μm for OCT imaging using the 370-nm-wide broadband source.

In addition, the operation wavelengths for OCT are also critical. For applications of OCTs in ophthalmology, light sources with central wavelength around 800 nm are widely used. As a result of the relatively short wavelength, ultra-high-resolution OCT can be easily obtained. However, a longer wavelength is desirable for increasing the penetration depth of the OCT. Ultra-high-resolution OCT in bio-tissue has been demonstrated with the SC source at the central wavelength of approximately 1, 1.3, 1.5, and 1.7 μm [55–57]. Water exhibits a broad absorption peak at 1.5 μm. Since biological materials are water rich, 1.5-μm light sources, highly developed for the optical communication industry, are not so suitable for OCT. *In vivo* OCT imaging in bio-tissues is thus typically performed at 1300 nm to take advantage of reduced scattering and enhanced penetration depth.

Moreover, for imaging of the cornea and anterior segment of the eye, OCT operated at 1300 nm has important potential advantages for glaucoma evaluation and refractive surgery [58]. The window around 1300 nm is particularly well suited for evaluation in detail of the response of the angle structures to light accommodation, which is an important part of the glaucoma workup.

Using rare-earth-doped fiber lasers, especially Yb-doped fiber lasers operating at high pulse energy with ultrashort pulse width (from tens to hundreds of femtoseconds) as the pump laser, new SC sources with a broad spectral bandwidth and high output power were reported by several groups [23–25]. Typically, PCF or highly nonlinear fiber is employed to generate SC in these schemes. The former approach provides higher nonlinearity and allows one to blue-shift the zero-dispersion wavelength [19].

Later, our group and others demonstrated [38, 39] that amplified NLPs could be successfully used for SCG through standard SMFs. NLPs [5, 9, 10, 59–62] exhibit attractive features such as a very smooth and broadband spectrum, a double-scaled autocorrelation trace with a sub-picosecond peak riding, and a wide sub-nanosecond pedestal, suggesting their low temporal coherence. It is conceivable that a SC source based on NLPs is potentially attractive for applications based on low-coherence interferometry such as OCT. In this work, we report for the OCT imaging with a new and improved SC source pumped by NLPs from a compact ANDi Yb-doped fiber laser.

NLPs from the ANDi Yb-doped fiber laser with an average power of 200 mW (pulse energy of 62.5 nJ) are first amplified through an Yb-doped fiber amplifier. The amplified NLPs are then used to excite the SC in a 50-m length of the standard SMF. At a pump power of 4.5 W, we are able to generate a flat SC spectrum at the central wavelength of 1320 nm with a spectral bandwidth of up to 420 nm (in 3-dB bandwidth), as shown in Figure 23. The average output power reaches up to 560 mW (pulse energy of 175 nJ).

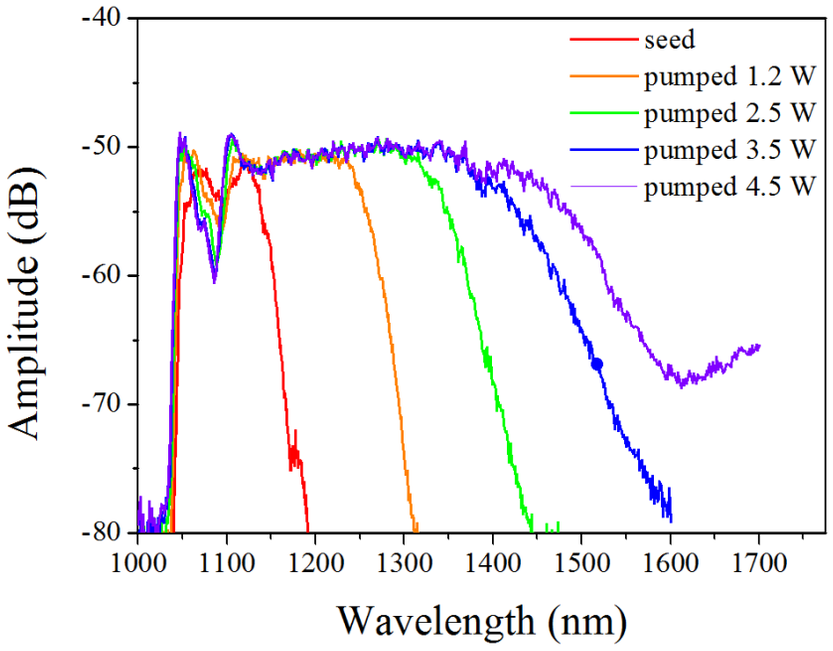

Figure 23. The SC spectra generated by an all-normal dispersion fiber laser system.

4.1. Time-domain OCT

To test whether our SC source is applicable to ultra-high-resolution OCT, we set up a simple OCT system. The system setup is similar to the Michelson interferometer as shown in Figure 24(a). There is a movable mirror in the reference arm, which directly reflects the light and changes the relative optical path length compared with the sample arm. Finally, the detector will receive the reflected light from two arms. At the sample arm, we assume the sample to have an inner structure with many layers, i.e., different refractive index variations, so the light will reflect back to the beam splitter and then be focused to the photodetector by focusing lens with different time delays. Using a pulse as the light source, we can observe the interferogram by oscilloscope. The interferogram provides the information about the position of the interface of the sample by different time delays corresponding to different positions of a movable mirror. The measured results can be understood from Figure 24(b).

4.2. Spectral-domain OCT

The spectral-domain approach for detection of OCT images is also referred to as the Fourier-domain OCT. The schematic of a spectral-domain OCT in shown in Figure 25(a) [49]. It can be immediately recognized that the movable mirror in TD-OCT is replaced by a stationary one. The photodetector is replaced by the spectrometer. The interferogram will be spectrally modulated and the wavelength dependence can be measured using a spectrometer (Figure 25(b)). We note that the optical path length mismatch ΔL must not be equal to zero during detection.

http://dx.doi.org/10.5772/61856

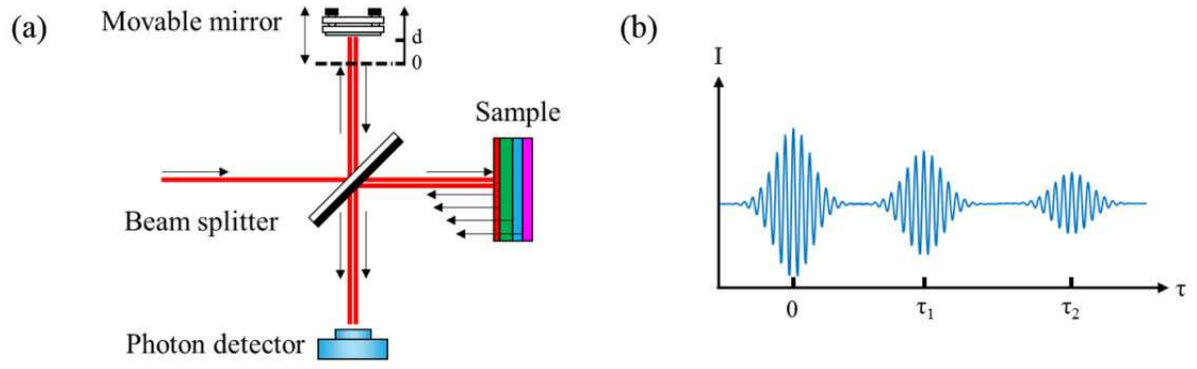

Figure 24. (a) The interferometer within an OCT system, and (b) the interferogram from an OCT system in time domain detection.

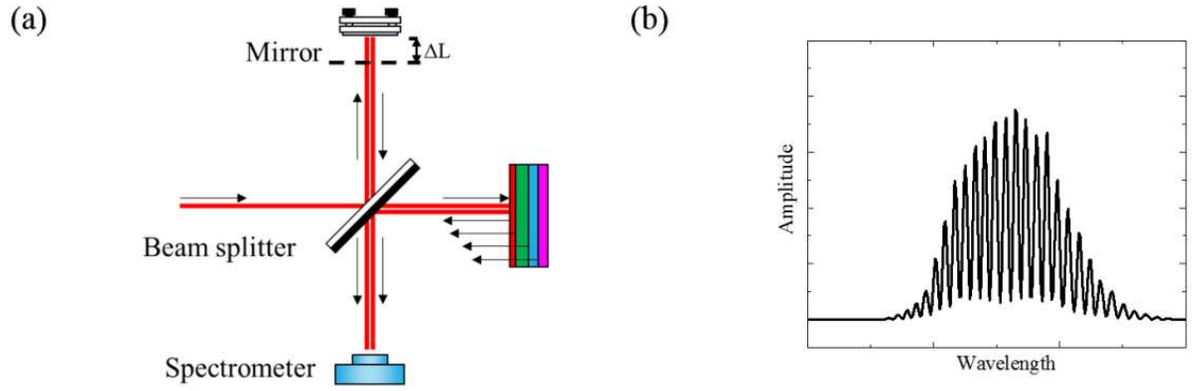

Figure 25. (a) The interferometer within an OCT system, and (b) the interferogram from an OCT system in spectral-/Fourier-domain detection.

4.3. OCT performance

Coherence length is a critical parameter for the OCT light source. The coherence length can be defined as the maximum path difference between reference and sample arms for which signals from both arm can interfere with each other. The coherence length of a source is related to the axial resolution of the OCT through

$$l_c = \frac{2\ln 2}{\pi}\frac{\lambda_0^2}{\Delta\lambda} \approx 0.44\frac{\lambda_0^2}{\Delta\lambda} \tag{5}$$

where $\Delta\lambda$ is the 3 dB bandwidth of optical spectrum and λ_0 is the central wavelength.

In this experiment, the SC light source generated an output power of around 345 mW, which is much higher than that of typical SC sources. With the SC source operated at a bandwidth of 365 nm center around 1320 nm, the theoretical axial resolution of the instrument is estimated to be ~2.1 μm. Figure 26(a) shows A-scan result of the TD-OCT. This corresponds to a measured

axial resolution of ~2.3 μm (Figure 26(b)). In spite of the ultra-high axial resolution provided by the TD-OCT, its signal-to-noise ratio (SNR) was only 12.5 dB. SD-OCT, on other hand, provides much better SNR and stability and quick scanning speed. Figure 27(a) shows the point-spread function (PSF) of the SD-OCT. An axial resolution of ~2.8 μm was achieved. In Figure 27(b), we show the PSFs of a free-space SD-OCT obtained at different depths. The data indicate that the system can provide OCT images at a depth of ~800 μm.

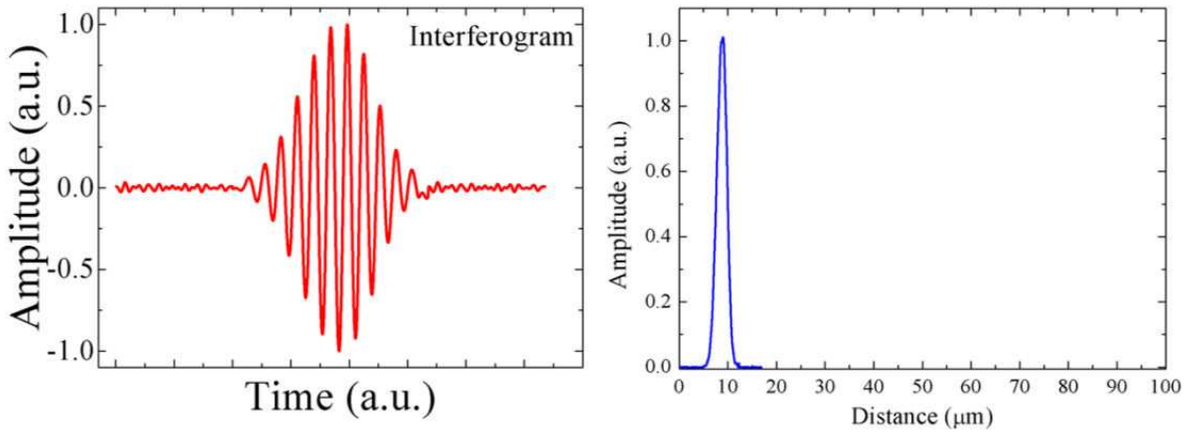

Figure 26. (a) A-scan result of the TD-OCT and (b) PSF.

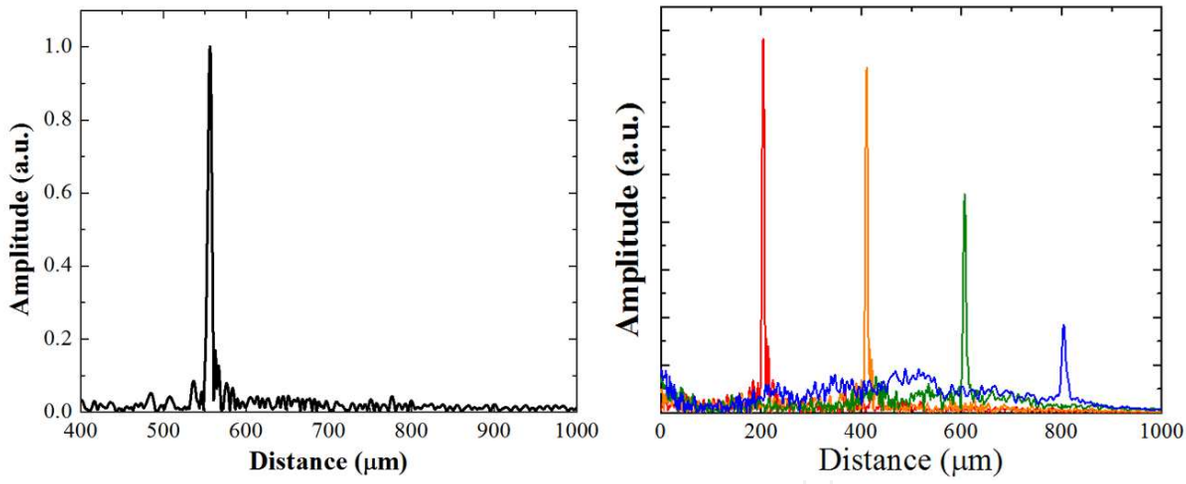

Figure 27. (a) PSF of SD-OCT and (b) PSFs at different depths.

Comparing with the free-space OCT, the fiber-based OCT is more compact and stable. Thus, results for the fiber-based spectral domain OCT system are also presented herein. Configuration of the fiber-based SD-OCT is shown schematically in Figure 28. The SC source was sent into a fiber coupler where it had a splitting ratio of 1:99. After the first fiber coupler, two optical fiber circulators are used in each arm. One arm serves as the reference, while the other arm delivers the signal to the sample. Afterwards, reflected light from the reference mirror and the

http://dx.doi.org/10.5772/61856

sample combine together using a second fiber coupler with a splitting ratio of 1:1. Finally, the interference signal is detected using an optical spectrum analyzer.

Our broadband SC source can achieve an ultra-high-resolution of ~ 2 μm. That of the all-fiber SD-OCT is limited, however, by the optical bandwidth of fiber components of the OCT system, such as optical circulators and optical couplers designed for the central wavelength of 1310 nm. Owing to that limitation, the effective spectral bandwidth for the fiber OCT system was only 102 nm. Therefore, the theoretical axial resolution of our all-fiber SD-OCT is ~5.3 μm. Figure 29(a) shows the PSF with and without dispersion compensation. The resolutions are 18.6 and 6.4 μm, respectively. It is apparent that the resolution is improved by dispersion compensation. Figure 29(b) shows the A-scan results obtained at different depths. The data were processed by applying the inverse Fourier transform to the measured interferograms. Our results indicate that the scanning depth can reach 1 mm. The SNR also improved significantly, reaching as high as 126.7 dB.

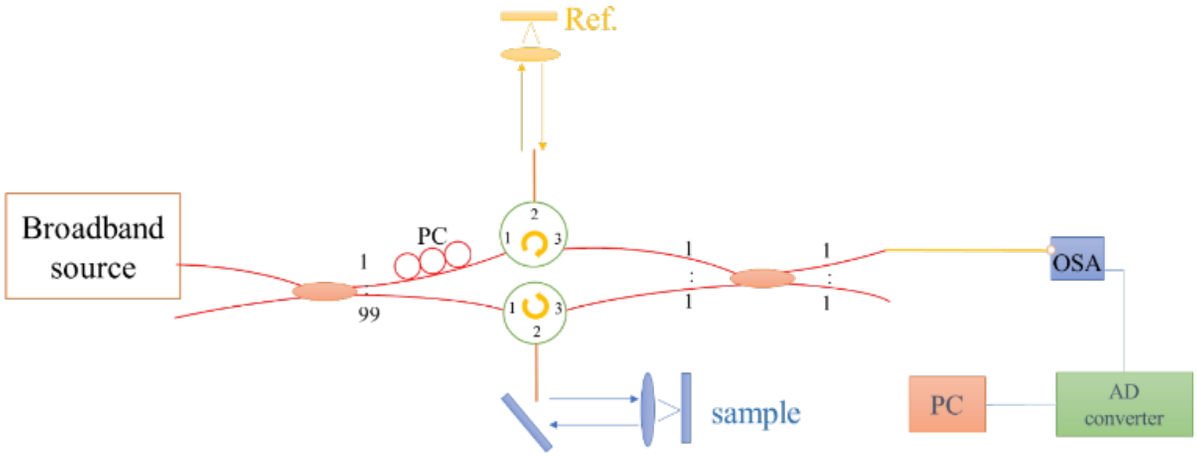

Figure 28. The schematic of SD-OCT system. PC, polarization controller; OSA, optical spectrum analyzer.

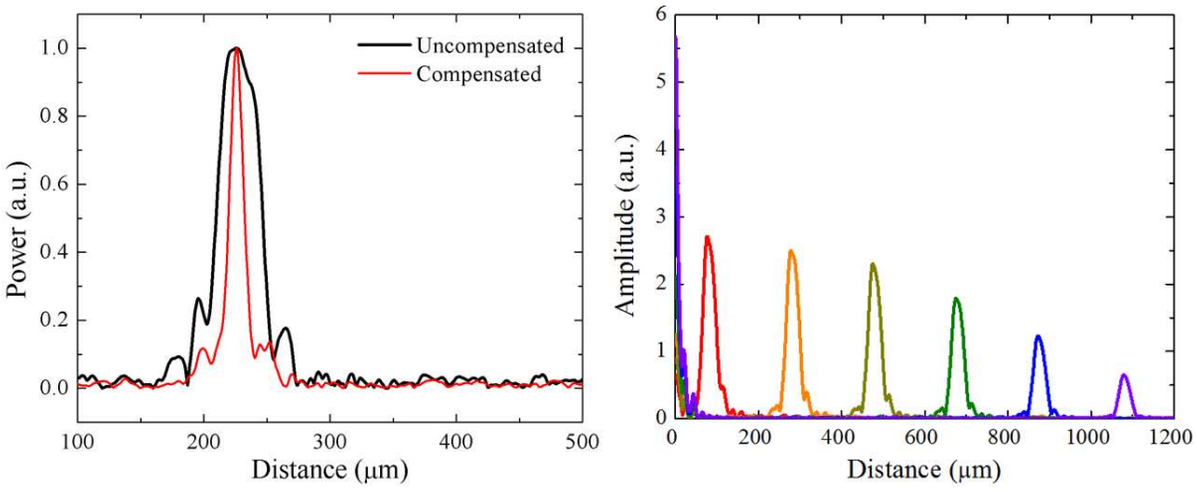

Figure 29. (a) The PSF with and without dispersion compensation. (b) A-scans at different depths.

4.4. OCT images

The surface tomography of a part of the one-dollar (new Taiwan dollar) coin is shown in Figure 30. In this case, the wavelength range of the source was ~45 nm, and the axial resolution was experimentally determined to be <17 μm. The OCT resolution is sufficient to get a clear image of the Chinese character, meaning "middle". The scanning step was 50 μm.

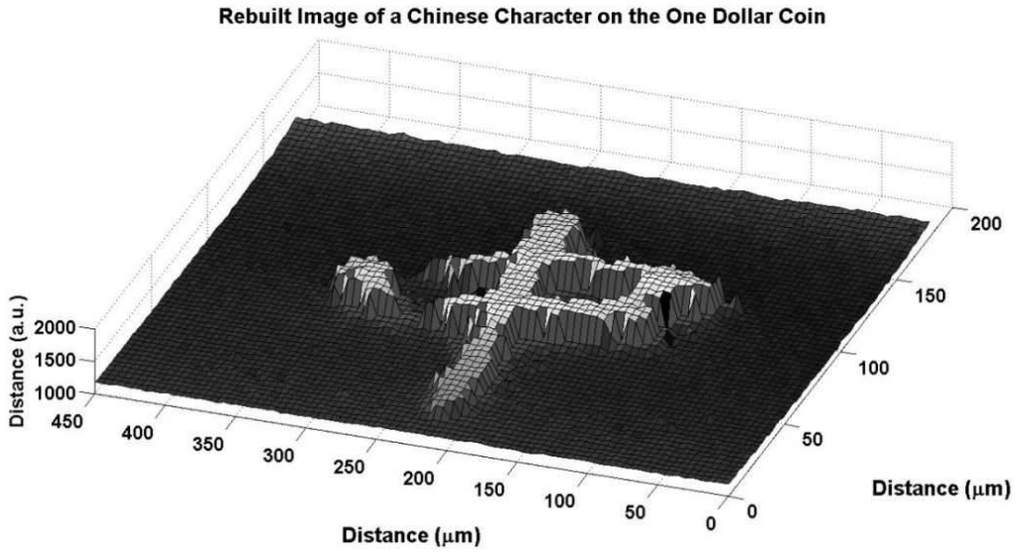

Figure 30. Image of a Chinese character "" on the coin of new Taiwan dollar.

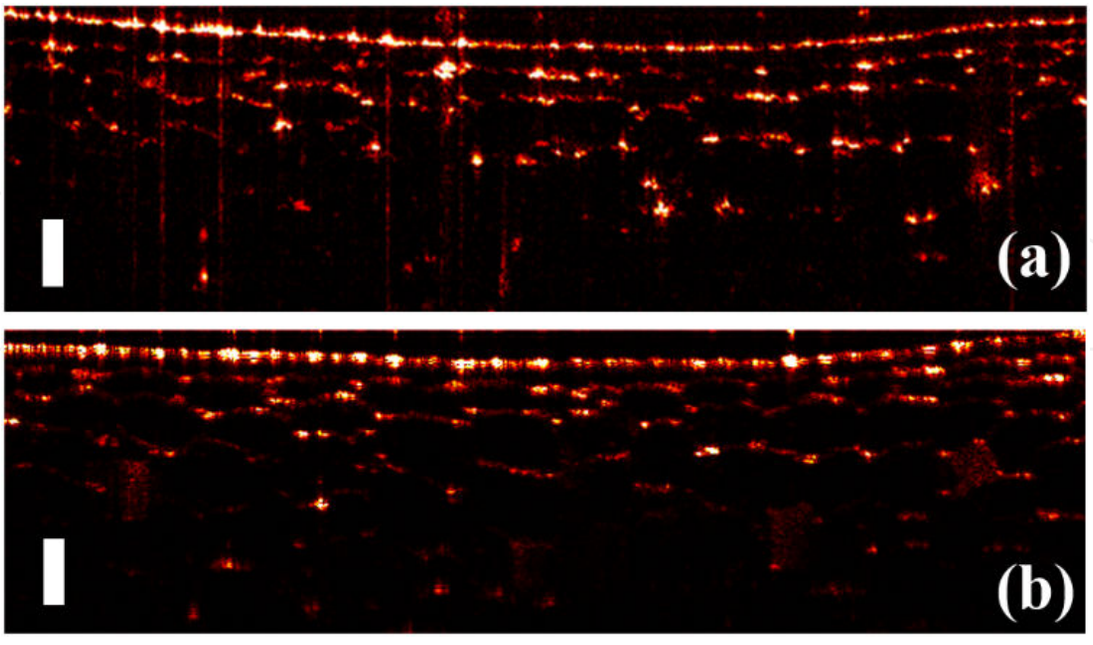

Figure 31. (a) SD-OCT image of an onion skin using a NLP laser. (b) SS-OCT image using a commercial swept source made by Santec. The scale bars represent 200 μm.

http://dx.doi.org/10.5772/61856

Figure 31 shows the OCT images of a layer of peeled onion skin using different light sources. Figure 31(a) is an image obtained with the fiber-based SD-OCT system using our noise-like SC light source, for which spectral bandwidth was limited by the fiber components as 108 nm. For comparison, Figure 31(b) is the OCT image obtained using the swept-source OCT (SS-OCT) system with a commercial swept source by Santec. The 2-D depth profile of the onion skin is obtained using both light sources. Several cell walls on onion skin can be easily identified. The best OCT images of the onion cell were obtained when we applied noise-like SC as a scan light source. The result of Figure 31(a) is the original image without dispersion compensation. This showed that higher image quality can be achieved through further data processing.

5. Summary

In this chapter, we describe our work on generation and amplification of medium- and high-energy NLPs with Yb-doped fiber laser systems. In the dispersion-mapped fiber laser system, the central wavelength and spectral bandwidth can be tuned. The tuning range was 33 nm and the bandwidth can be varied from 6 to 54 nm. Stable NLPs can be generated with output power from 0.1 to 1.6 W, limited by damage of the optical fiber components used. Pulse energy as high as 1. 25 μJ can be generated directly from the laser oscillator with a repetition rate of ~1 MHz. On the other hand, the ANDi noise-like fiber laser is more compact and can generate broadband NLPs with a bandwidth as high as ~80 nm. We also demonstrate SCG pumped by NLPs in easily available single-mode optical fibers. SC with a flat spectrum can be generated over 420 nm in 3-dB bandwidth, centered around 1.3 μm. Such broad spectrum arises from cascaded stimulated Raman scattering and self-phase modulation in the optical fibers. SMFs with high nonlinearity can be used to generate even broader spectra. Significant modulations due to the nonlinear effects rendered such sources unsuitable OCT. Experimental results are in good agreement with theoretical analysis and numerical simulation results. SC pumped by NLPs has been employed successfully in OCT systems. An ultra-high axial resolution of 2.3 μm was demonstrated. High-resolution fiber-based spectral domain OCT is also demonstrated. Scanned images show that a SC source pumped by NLPs is a viable alternative to SLD and SC pumped by femtosecond lasers as the broadband light source for applications such as OCT.

Acknowledgements

This work was supported in part by the Ministry of Science and Technology, Taiwan, under Grant 103-2622-E-007-006-CC2 and by the National Tsing Hua University Research Program Grant 104N2711E1. C. L. Pan is also supported by the Air Force Office of Scientific Research FA2386-13-1-4086. Some of the experimental results presented in this chapter were obtained through collaboration with Prof. Ping Xue and Mr. Chengming Wang, Tsinghua University, Beijing. We also gratefully acknowledge Yi-Lun Lin and Kuo-Sung Huang for their contributions to the work summarized in this chapter.

Author details

Ci-Ling Pan*, Alexey Zaytsev, Yi-Jing You and Chih-Hsuan Lin

*Address all correspondence to: clpan@phys.nthu.edu.tw

National Tsing Hua University, Hsinchu, Taiwan, R.O.C.

References

[1] Barnard C, Myslinski P, Chrostowski J, Kavehrad M. Analytical model for rare-earth-doped fiber amplifiers and lasers. IEEE J. Quantum Electron. 1994;30:1817–1830. DOI: 10.1109/3.301646

[2] Stone J, Burrus CA. Neodymium-doped fiber lasers: room temperature CW operation with an injection laser pump. Appl. Opt. 1974;13:1256–1258. DOI: 10.1364/AO.13.001256

[3] Barnes WL, Poole SB, Townsend JE, Reekie L, Taylor DJ, Payne DN. "Er^{3+}-Yb^{3+} and Er^{3+} doped fiber lasers. J. Lightwave Technol. 1989;7:1461–1465. DOI: 10.1109/50.39081

[4] Pottiez O, Grajales-Coutino R, Ibarra-Escamilla B, Kuzin EA, Hernandez-Garcia JC. Adjustable noiselike pulses from a figure-eight fiber laser. Appl. Opt. 2011; 50:E24–E31. DOI: 10.1364/AO.50.000E24

[5] Kobtsev S, Kukarin S, Smirnov S, Turitsyn S, Latkin A. Generation of double-scale femto/pico-second optical lumps in mode-locked fiber lasers. Opt. Exp. 2009;17:20707–20713. DOI: 10.1364/OE.17.020707

[6] An Y, Shen D, Zhao W, Long J. Characteristics of pulse evolution in mode-locked thulium-doped fiber laser. Opt. Commun. 2012;285:1949–1953. DOI: 10.1016/j.optcom.2011.12.001

[7] Kobtsev S, Smirnov S. Fiber lasers mode-locked due to nonlinear polarization evolution: golden mean of cavity length. Laser Phys. 2011;21:272–276. DOI: 10.1134/S1054660X11040050

[8] Zhao L, Tang D, Wu J, Fu X, Wen S. Noise-like pulse in a gain-guided soliton fiber laser. Opt. Exp. 2007;15:2145–2150. DOI: 10.1364/OE.15.002145

[9] Horowitz M, Barad Y, Silberberg Y. Noiselike pulses with a broadband spectrum generated from an erbium-doped fiber laser. Opt. Lett. 1997;22:799–801. DOI: 10.1364/OL.22.000799

[10] Smirnov S, Kobtsev S, Kukarin S, Ivanenko A. Three key regimes of single pulse generation per round trip of all-normal-dispersion fiber lasers mode-locked with nonlinear polarization rotation. Opt. Exp. 2012;20:27447–27453. DOI: 10.1364/OE.20.027447

[11] Tang D, Zhao L, Zhao B. Soliton collapse and bunched noise-like pulse generation in a passively mode-locked fiber ring laser. Opt. Exp. 2005;13:2289–2294. DOI: 10.1364/OPEX.13.002289

[12] Smirnov SV, Kobtsev SM, Kukarin SV. Efficiency of non-linear frequency conversion of double-scale pico-femtosecond pulses of passively mode-locked fiber laser. Opt. Exp. 2014;22:1058–1064. DOI: 10.1364/OE.22.001058

[13] Aguergaray C, Runge A, Erkintalo M, Broderick NG. Raman-driven destabilization of mode-locked long cavity fiber lasers: fundamental limitations to energy scalability. Opt. Lett. 2013;38:2644–2646. DOI: 10.1364/OL.38.002644

[14] Zaytsev A, Lin CH, You YJ, Tsai TF, Wang CL, Pan CL. A controllable noise-like operation regime in a Yb-doped dispersion-mapped fiber ring laser. Laser Phys. Lett. 2013;10:045104. DOI: 10.1088/1612-2011/10/4/045104

[15] Lim H, Ilday FÖ, Wise FW. Generation of 2-nJ pulses from a femtosecond ytterbium fiber laser. Opt. Lett. 2003;28:660–662. DOI: 10.1364/OL.28.000660

[16] Agrawal GP. Nonlinear fiber optics. 5th ed. Waltham: Elsevier/Academic; 2013. DOI: 10.1016/B978-0-12-397023-7.00011-5

[17] Pan CL, Zaytsev A, Lin CH, You YJ, Wang CH. Progress in short-pulse Yb-doped fiber oscillators and amplifiers. In: Lee CC, editor. The current trends of optics and photonics. Dordrecht: Springer; 2015. pp. 61–100. DOI: 10.1007/978-94-017-9392-6_3

[18] Chong A, Buckley J, Renninger W, Wise FW. All-normal-dispersion femtosecond fiber laser. Opt. Exp. 2006;14:10095–10100. DOI: 10.1364/OE.14.010095

[19] Dudley JM, Genty G, Coen S. Supercontinuum generation in photonic crystal fiber. Rev. Mod. Phys. 2006;78:1135–1184. DOI: 10.1103/RevModPhys.78.1135

[20] Bizheva K, Považay B, Hermann B, Sattmann H, Drexler W, Mei M, Holzwarth R, Hoelzenbein T, Wacheck V, Pehamberger H. Compact, broad-bandwidth fiber laser for sub-2-μm axial resolution optical coherence tomography in the 1300-nm wavelength region. Opt. Lett. 2003;28:707–709. DOI: 10.1364/OL.28.000707

[21] Diddams SA, Jones DJ, Ye J, Cundiff ST, Hall JL, Ranka JK, Windeler RS, Holzwarth R, Udem T, Hansch TW. Direct link between microwave, and optical frequencies with a 300 THz femtosecond laser comb. Phys. Rev. Lett. 2000;84:5102–5105. DOI: 10.1103/PhysRevLett.84.5102

[22] Boivin L, Collings BC. Spectrum slicing of coherent sources in optical communications. Opt. Fiber Technol. 2001;7:1–20. DOI: 10.1006/ofte.2000.0342

[23] Song R, Hou J, Chen S, Yang W, Lu Q. High power supercontinuum generation in a nonlinear ytterbium-doped fiber amplifier. Opt. Lett. 2012;37:1529–1531. DOI: 10.1364/OL.37.001529

[24] Hu X, Zhang W, Yang Z, Wang Y, Zhao W, Li X, Wang H, Li C, Shen D. High average power, strictly all-fiber supercontinuum source with good beam quality. 2011;36:2659–2661. DOI: 10.1364/OL.36.002659

[25] Chen H, Chen Z, Chen S, Hou J, Lu Q. Hundred-watt-level, all-fiber-integrated supercontinuum generation from photonic crystal fiber. Appl. Phys. Exp. 2013;6:032702-1-3. DOI: 10.7567/APEX.6.032702

[26] Alfano RR, Shapiro SL. Emission in the region 4000 to 7000 Å via four-photon coupling in glass. Phys. Rev. Lett. 1970;24:584–587. DOI: 10.1103/PhysRevLett.24.584

[27] Hernandez-Garcia JC, Pottiez O, Estudillo-Ayala JM, Rojas-Laguna R. Numerical analysis of a broadband spectrum generated in a standard fiber by noise-like pulses from a passively mode-locked fiber laser. Opt. Commun. 2012;285:1915–1919. DOI: 10.1016/j.optcom.2011.12.069

[28] Petropoulos P, Ebendorff-Heidepriem H, Finazzi V, Moore RC, Frampton K, Richardson DJ, Monro TM. Highly nonlinear and anomalously dispersive lead silicate glass holey fibers. Opt. Exp. 2003;11:3568–3573. DOI: 10.1364/OE.11.003568

[29] Ebendorff-Heidepriem H, Petropoulos P, Asimakis S, Finazzi V, Moore RC, Frampton K, Koizumi F, Richardson DJ, Monro TM. Bismuth glass holey fibers with high nonlinearity. Opt. Exp. 2004;12:5082–5087. DOI: 10.1364/OPEX.12.005082

[30] Liao M, Yan X, Qin G, Chaudhari C, Suzuki T, Ohishi Y. A highly non-linear tellurite microstructure fiber with multi-ring holes for supercontinuum generation. Opt. Exp. 2009;17:15481–15490. DOI: 10.1364/OE.17.015481

[31] Qin G, Yan X, Kito C, Liao M, Chaudhari C, Suzuki T, Ohishi Y. Ultrabroadband supercontinuum generation from ultraviolet to 6.28 μm in a fluoride fiber. Appl. Phys. Lett. 2009;95:161103. DOI: 10.1063/1.3254214

[32] El-Amraoui M, Gadret G, Jules JC, Fatome J, Fortier C, Désévédavy F, Skripatchev I, Messaddeq Y, Troles J, Brilland L, Gao W, Suzuki T, Ohishi Y, Smektala R. Microstructured chalcogenide optical fibers from As_2S_3 glass: towards new IR broadband sources. Opt. Exp. 2010;18:26655–26665. DOI: 10.1364/OE.18.026655

[33] Xiao L, Demokan MS, Jin W, Wang Y, Zhao CL. Fusion splicing photonic crystal fibers and conventional single-mode fibers: Microhole collapse effect. J. Lightwave Technol. 2007;25:3563–3574. DOI: 10.1109/JLT.2007.907787

[34] Pourbeyram H, Agrawal GP, Mafi A. Stimulated Raman scattering cascade spanning the wavelength range of 523 to 1750~nm using a graded-index multimode optical fiber. Appl. Phys. Lett. 2013;102:201107. DOI: 10.1063/1.4807620

[35] Yin K, Zhang B, Yang W, Chen H, Hou J. Over an octave cascaded Raman scattering in short highly germanium-doped silica fiber. Opt. Exp. 2013;21:15987–15997. DOI: 10.1364/OE.21.015987

[36] Sayinc H, Hausmann K, Morgner U, Neumann J, Kracht D. Picosecond all-fiber cascaded Raman shifter pumped by an amplified gain switched laser diode. Opt. Exp. 2011;19:25918–25924. DOI: 10.1364/OE.19.025918

[37] Ilev I, Kumagai H, Toyoda K, Koprinkov I. Highly efficient wideband continuum generation in a single-mode optical fiber by powerful broadband laser pumping. Appl. Opt. 1996;35:2548–2553. DOI: 10.1364/AO.35.002548

[38] Hernandez-Garcia JC, Pottieza O, Estudillo-Ayalab JM. Supercontinuum generation in a standard fiber pumped by noise-like pulses from a figure-eight fiber laser. Laser Phys. 2012;22:221–226. DOI: 10.1134/S1054660X1123006X

[39] Zaytsev A, Lin CH, You YJ, Chung CC, Wang CL, Pan CL. Supercontinuum generation by noise-like pulses transmitted through normally dispersive standard single-mode fibers. Opt. Exp. 2013;21:16056–16062. DOI: 10.1364/OE.21.016056

[40] Brückner V. Elements of optical networking. Basics and practice of optical data communication. Wiesbaden: Springer; 2011. DOI: 10.1007/978-3-8348-8142-7_8

[41] Rottwitt K, Povlsen JH. Analyzing the fundamental properties of Raman amplification in optical fibers. J. Lightwave Technol. 2005;23:3597–3605. DOI: 10.1109/JLT.2005.857776

[42] Blow KJ, Wood D. Theoretical description of transient stimulated Raman scattering in optical fibers. IEEE J. Quantum Electron. 1989;25:2665–2673. DOI: 10.1109/3.40655

[43] Kato T, Suetsugu Y, Nishimura M. Estimation of nonlinear refractive index in various silica-based glasses for optical fibers. Opt. Lett. 1995;20:2279–2281. DOI: 10.1364/OL.20.002279

[44] Lin C, Nguyen VT, French WG. Wideband near-I.R. continuum (0.7–2.1 μm) generated in low-loss optical fibers. Electron Lett. 1978;14:822–823. DOI: 10.1049/el:19780556

[45] Santhanama J, Agrawal GP. Raman-induced spectral shifts in optical fibers: general theory based on the moment method. Opt. Commun. 2003;222:413–420. DOI: 10.1016/S0030-4018(03)01561-X

[46] Huang D, Swanson EA, Lin CP, Schuman JS, Stinson WG, Chang W, Hee MR, Flotte T, Gregory K, Puliafito CA. Optical coherence tomography. Science. 1991;254:1178–1181. DOI: 10.1126/science.1957169

[47] Fercher AF, Hitzenberger CK, Drexler W, Kamp G, Sattmann H. In vivo optical coherence tomography. Am J. Ophthalmol. 1993;116:113–114. DOI: 10.5858/arpa.2012-0252-SA

[48] Swanson EA, Izatt J, Lin C, Fujimoto J, Schuman J, Hee M, Huang D, Puliafito C. In vivo retinal imaging by optical coherence tomography. Opt. Lett. 1993;18:1864–1866. DOI: 10.1364/OL.18.001864

[49] Izatt JA, Choma MA. Theory of optical coherence tomography. In: Drexler W, Fujimoto J, editors. Optical coherence tomography. Berlin Heidelberg: Springer; 2008. pp. 47–72. DOI: 10.1007/978-3-540-77550-8_2

[50] Fercher AF, Hitzenberger CK, Kamp G, El-Zaiat SY. Measurement of intraocular distances by backscattering spectral interferometry. Opt. Commun. 1995;117:43–48. DOI: 10.1016/0030-4018(95)00119-S

[51] Wojtkowski M, Leitgeb R, Kowalczyk A, Bajraszewski T, Fercher AF. In vivo human retinal imaging by Fourier domain optical coherence tomography. J. Biomed. Opt. 2002;7:457–463. DOI: 10.1117/1.1482379

[52] de Boer JF, Cense B, Park BH, Pierce MC, Tearney GJ, Bouma BE. Improved signal-to-noise ratio in spectral-domain compared with time-domain optical coherence tomography. Opt. Lett. 2003;28:2067–2069. DOI: 10.1364/OL.28.002067

[53] Leitgeb R, Hitzenberger C, Fercher A. Performance of fourier domain vs. time domain optical coherence tomography. Opt. Express. 2003;11:889–894. DOI: 10.1364/OE.11.000889

[54] Hartl I, Li XD, Chudoba C, Ghanta RK, Ko TH, Fujimoto JG, Ranka JK, Windeler RS. Ultrahigh-resolution optical coherence tomography using continuum generation in an air–silica microstructure optical fiber. Opt. Lett. 2001;26:608–610. DOI: 10.1364/OL.26.000608

[55] Kodach VM, Kalkman J, Faber DJ, van Leeuwen TG. Quantitative comparison of the OCT imaging depth at 1300 nm and 1600 nm. Biomed. Opt. Express. 2010;1:176–185. DOI: 10.1364/BOE.1.000176

[56] Lim H, Jiang Y, Wang Y, Huang YC, Chen Z, Wise FW. Ultrahigh-resolution optical coherence tomography with a fiber laser source at 1 μm. Opt. Lett. 2005;30:1171–1173. DOI: 10.1364/OL.30.001171

[57] Ishida S, Nishizawa N, Ohta T, Itoh K. Ultrahigh-resolution optical coherence tomography in 1.7 μm region with fiber laser supercontinuum in low-water-absorption samples. Appl. Phys. Express. 2011;4:052501. DOI: 10.1143/APEX.4.052501

[58] Choma MA, Hsu K, Izatt JA. Swept source optical coherence tomography using an all-fiber 1300-nm ring laser source. J. Biomed. Opt. 2005;10:044009. DOI: 10.1117/1.1961474

[59] Lecaplain C, Grelu PH. Rogue waves among noiselike-pulse laser emission: an experimental investigation. Phys. Rev. A. 2014;90:013805. DOI: 10.1103/PhysRevA.90.013805

[60] Hernandez-Garcia JC, Pottiez O, Grajales-Coutiño R, Ibarra-Escamilla B, Kuzin EA, Estudillo-Ayala JM, Gutierrez-Gutierrez J. Generation of long broadband pulses with a figure-eight fiber laser. Laser Phys. 2011;21:1518–1524. DOI: 10.1134/S1054660X11150114

[61] Jeong Y, Vazquez-Zuniga LA, Lee S, Kwon Y. On the formation of noise-like pulses in fiber ring cavity configurations. Opt. Fiber Technol. 2014;20:575–592. DOI: 10.1016/j.yofte.2014.07.004

[62] Suzuki M, Ganeev RA, Yoneya S, Kuroda H. Generation of broadband noise-like pulse from Yb-doped fiber laser ring cavity. Opt. Lett. 2015;40:804–807. DOI: 10.1364/OL.40.000804

IntechOpen